Numerical Study of Convection Observed during the Winter Monsoon Experiment Using a Mesoscale Two-Dimensional Model

JIMY DUDHIA

Department of Meteorology, The Pennsylvania State University, University Park, Pennsylvania

(Manuscript received 14 October 1988, in final form 8 May 1989)

ABSTRACT

A two-dimensional version of the Pennsylvania State University mesoscale model has been applied to Winter Monsoon Experiment data in order to simulate the diurnally occurring convection observed over the South China Sea.

The domain includes a representation of part of Borneo as well as the sea so that the model can simulate the initiation of convection. Also included in the model are parameterizations of mesoscale ice phase and moisture processes and longwave and shortwave radiation with a diurnal cycle. This allows use of the model to test the relative importance of various heating mechanisms to the stratiform cloud deck, which typically occupies several hundred kilometers of the domain. Frank and Cohen's cumulus parameterization scheme is employed to represent vital unresolved vertical transports in the convective area. The major conclusions are:

(i) Ice phase processes are important in determining the level of maximum large-scale heating and vertical motion because there is a strong anvil component. The heating is initiated by a thermodynamic adjustment that takes place after the air leaves the updrafts and is associated with the difference between water and ice saturation.

(ii) Melting and evaporation contribute to a localized mesoscale subsidence in a 50 km region to the rear of the moving convective area. The cooling associated with this almost cancels the cumulus heating in the lower to midtroposphere.

(iii) Radiative heating was found to be the main ascent-forcing influence at high levels occupied by the widespread cirrus outflow. Additionally, radiative clear-air cooling helped the convection by continuously destabilizing the troposphere and countering the warming effect of convective updrafts.

(iv) The overall structure and development of the system were well simulated, particularly the growth near the coast, and the propagation and decay in the cooler boundary layer further off-shore, but the rainfall may have been underestimated because of the two-dimensional assumptions of the model.

1. Introduction

During the Northern Hemisphere's winter, the most convectively active region in the tropics is the "maritime continent," a region including Malaysia, Indonesia, and Borneo. This region has the strongest vertical mass flux and represents the upward branch of both latitudinal (Hadley) and longitudinal (Walker) circulations. The combination of moisture from the maritime tropical air and surface heating from the land make this region particularly favorable for convection, and hence for driving a monsoon circulation during the winter months.

The Winter Monsoon Experiment (WMONEX) was carried out in December 1978–February 1979 with the aim of understanding the convective behavior of the maritime continent in more detail. Particular emphasis was given to the region northwest of Borneo, which represents the center of the winter monsoon activity and is part of the near-equatorial trough.

Three Soviet ships in the South China Sea, together with a weather radar at Bintulu, on the northwest coast of Borneo, and aircraft provided detailed observations throughout the period 5–31 December 1978.

The most distinct feature of convection in the South China Sea is its diurnal cycle, which persists in the presence of larger scale disturbances in the flow resulting from cold surges and equatorial easterly waves (Houze et al. 1981, Johnson and Priegnitz 1981). Houze et al. (1981) present time sequences and composites of cloud area and rainfall for 8–31 December 1978 and proposed a conceptual model for the South China Sea convective behavior. The northeasterly monsoon flow is almost parallel to the coastline during this season. According to the conceptual model, a nighttime land breeze forms in response to the cooling of the Borneo land surface, and, although this is weak, it is capable of providing sufficient convergence around 0000 to 0200 Local Solar Time (LST) to initiate convection just offshore. The monsoonal flow at low levels

Corresponding author address: Dr. Jimy Dudhia, Mesoscale and Microscale Meteorology Division, NCAR, Boulder, CO 80307-3000.

is close to thermodynamic equilibrium with the warm underlying ocean, and there is conditional instability. Once convection is initiated, it seems to sustain itself by convergence associated with cold convective outflow at the surface. New cells form where this convective outflow meets the monsoon flow, and the system propagation is determined partly by the upper level offshore wind component. Johnson and Priegnitz (1981) estimate this propagation to be about 6 m s^{-1} towards the west–northwest. The system eventually dissipates when it encounters less favorable thermodynamic conditions several hundred kilometers from the Borneo coast. This stage occurs after about 1000 LST.

Churchill and Houze (1984a) give a detailed account of the structure of the 10 December 1978 case that occurred at the onset of a cold surge. The mature stage of this cluster, 0600–0800 LST, is marked by a broad area of stratiform precipitating cloud, 100–200 km across, in which convective cores are embedded. These cores are concentrated on the upwind (relative to the northeasterly monsoon low-level flow) side of the stratiform region as well as near the coast, possibly as a result of continuing land-breeze convergence there. The center of the rainfall, as detected by radar (Houze et al. 1981), moves away from the coast, indicating that the cores nearer the coast during the mature stage are weak, and those responsible for mesoscale anvil cloud form to its north and northwest.

Churchill and Houze (1984a) also present microphysical data on the particle types in these clouds. A main result is that the core regions are associated mostly with rimed particles, and growth occurs by mixed phase (ice and water) processes. In the stratiform region particle habits are branched, so growth is primarily by vapor deposition and aggregation in supersaturated conditions with respect to ice with little evidence of riming. They estimate that about 46% of the precipitation from the 10 December case was stratiform. This system is thus typical of many clusters found in tropical regions because it has mesoscale and convective-scale components that are clearly distinguishable by their microphysics and dynamics (vertical motion strengths) and contribute almost equally to the surface rainfall. Squall lines observed in the east tropical Atlantic (GARP Atlantic Tropical Experiment, GATE), e.g., by Gamache and Houze (1982), Zipser (1977); in West Africa by Sommeria and Testud (1984); and cloud clusters in the recent Equatorial Mesoscale Experiment (EMEX) near North Australia, all exhibit these two scales of motion, each with significant precipitation production.

Associated with the mesoscale cloud is a heating profile that strongly influences the overall heating of the cluster. Johnson and Young (1983) analyzed several WMONEX clusters' heating profiles, derived from ship rawinsonde data, and show a consistent time development where the heating maximum shifts upward, and a lower tropospheric cooling dominates at later stages in the clusters' lifetime. This development of the heating profile corresponds to an almost simultaneous development in mesoscale vertical motion, where in later stages upper tropospheric mesoscale ascent and lower tropospheric mesoscale descent exist. Similar mesoscale updraft magnitudes of a few tens of centimeters per second are found in the GATE cases studied by Houze (1982), Gamache and Houze (1982), and Houze and Rappaport (1984); in the West African case of Chong et al. (1987); and in WMONEX (Johnson and Young 1983 and Churchill and Houze 1984b).

While it is clear that the mesoscale motion field in these tropical systems is largely dependent on the heating profile, it is not clear which processes dominate the heating profile on these scales of several hundred kilometers. Webster and Stephens (1980) point out that radiative effects tend to warm cloud base relative to cloud top, thus destabilizing the cloud layer while also offsetting the cooling due to melting at cloud base, which is at the freezing level (5 km). Also, net radiative heating within some cloud layers of up to 10 K d^{-1} can be almost half of the value typically diagnosed from heat budgets (such as Johnson and Young's 1983) and so is not negligible.

Leary and Houze (1979) suggest that melting and evaporation of about 20 K d^{-1} occurs below stratiform cloud decks, and Brown (1979), in a numerical modeling study of mesoscale cloud regions using a midlatitude sounding, shows the importance of evaporation in sustaining the downward motion in the lower troposphere. However, the upper troposphere is more complicated because the sounding within the mesoscale cloud is likely to be near neutral with respect to moist or frozen ascent, as suggested by Johnson and Kriete (1982), and is thus susceptible to large vertical motions even for small amounts of additional latent or radiative heating.

Brown's modeled stratiform region produced updrafts that detrained water-loaded cloudy air at their level of neutral buoyancy and then released rainwater and gained a positive buoyancy, resulting in mesoscale ascent. Cohen and Frank (1987) also produce mesoscale ascent in a GATE slow-moving line simulation. They demonstrate that lateral detrainment of updraft air at midlevels was an essential factor in destabilizing the upper troposphere. These mechanisms, together with Webster and Stephens' radiative destabilization and the probably important ice phase processes (discussed in section 3) are all small effects in terms of heating, but are made dynamically important by taking place in nearly neutral stratification with respect to saturated motion.

Another radiative mechanism proposed by Gray and Jacobsen (1977) may also contribute to ascent in the cloudy region. They suggest that the clear air around the clouds cools more than the cloudy region, particularly at night due to longwave radiative effects, and this may induce weak low-level convergence into the

cloudy region. The early morning is the most favorable time for such convergence, but this effect is expected to be weak compared to the land-breeze and applies more to convection far from land.

From the evidence presented above, it seems that to represent WMONEX systems properly in a numerical model, there are several requirements that should be met. First, the model should include a realistic convective cloud scheme, because convective transports of heat and moisture initiate mesoscale cloud development. Second, the model requires a microphysical scheme capable of reproducing the observed ice-dominated stratiform clouds and their associated latent heating. Third, a radiative transfer scheme is needed to determine the impact of longwave and shortwave heating.

A hydrostatic two-dimensional model will be used to simulate the basic features of WMONEX systems taking into account the above-mentioned processes. The primary advantage of using a hydrostatic model is its efficiency compared with nonhydrostatic models for mesoscale simulations, allowing more tests and sensitivity studies on new schemes added to the model. However, the horizontal grid length of 10 km requires the incorporation and testing of a cumulus parameterization scheme to represent convective-scale transports, which adds to the task. The application of a cumulus parameterization scheme to this grid scale may be questionable, but the range of convective strengths, for which the model behaves realistically, has been tested and the limit of validity appears not to be exceeded in the simulations (as will be demonstrated).

In this paper the basic model is presented in section 2. The ice phase and radiative transfer parameterizations are examined in sections 3 and 4 respectively, and the schemes are tested in idealized one-dimensional (horizontally uniform) conditions to determine their potential effects on the model. Section 5 provides a brief description of the cumulus parameterization scheme and the considerations required in interfacing it with the model. This is followed by a description of the particular observed case in WMONEX and the method by which the model is initialized to simulate it (section 6). In section 7, the simulation results are presented, followed by a discussion of the relative importance of various physical processes on the heating profile and on the dynamics of the simulated system (section 8). A comparison with the observations of WMONEX is provided in section 9.

2. Mesoscale model

a. Numerical methods

The two-dimensional "research" version of the Penn State hydrostatic mesoscale model was used and modified for these studies.

The basic equations from Anthes and Warner (1978) are given in appendix A. The coordinate system is σ-pressure coordinates defined to be 1 at the surface and 0 at the top of the domain, which is a constant pressure surface (50 hPa in this case). The advantage of these coordinates is the ease with which topography can be included. The model levels are constant σ surfaces.

Prognostic equations exist for surface pressure, the two horizontal momentum components, temperature, water vapor, cloud water, and rain water together with diagnostic equations for vertical motion (from continuity) and height of the σ-surfaces (hydrostatic equation). Ice and snow are incorporated (as discussed later) in the cloud and rain fields without requirement of additional storage.

The time differencing scheme is the second order centered leapfrog method with the exception of spatial diffusion terms which, for stability, are evaluated by the first order forward step. There is a time filter on all variables to prevent solution splitting, and the Brown and Campana (1978) method is employed to aid stability with longer time steps. This method basically uses a semi-implicit "temporally diffused" horizontal pressure gradient in the momentum equation rather than the time-centered value.

Spatial differencing is second order centered apart from rainfall, which is calculated with a first order upstream scheme. A fourth order derivative horizontal (along pressure surfaces) diffusive term is applied to all prognostic variables to suppress two-grid-length waves.

The horizontal grid length is 10 km and there are 18 equally spaced σ-levels between the surface and 50 hPa. Thus the lowest layers are about 470 m thick, and at 400 hPa they are about 1 km thick. The time step is limited to 10 seconds and the domain covers 700 km.

The lateral boundaries allow inflow and outflow, and the surface pressure at the boundary points is damped towards its initial value to prevent tendencies from developing in the domain's total mass. The top boundary is a pressure surface with no flow across it ($\omega = 0$).

b. Physical parameterizations

There are both marine and land surfaces within the domain, together with simplified terrain up to 500 m altitude. The surface interacts with the atmosphere through frictional effects and heat and moisture fluxes. It also provides a boundary longwave flux for the radiative tranfer scheme (discussed later). Following Anthes and Warner (1978), the land surface temperature varies according to radiative heating or cooling, fluxes of sensible and latent heat into the atmosphere, and the heat flux into the subsurface layer by downward diffusion. The ocean temperature is specified according to observations and kept constant.

It is necessary for the boundary layer to have the correct qualitative response to the diurnal heating cycle because of the land breeze observed during WMONEX

(Houze et al. 1981) that is thought to be responsible for the initial formation of convection near the coast. A bulk planetary boundary layer scheme is used (described in appendix A).

The model has both a convective parameterization and an explicit moisture scheme. Convective parameterization is necessary to represent subgrid-scale transports by updrafts and downdrafts, which vertically redistribute heat, moisture, and momentum within model resolved columns and also produce convective rainfall. Such processes cannot be left to the resolved-scale advection, as discussed by Zhang et al (1988), since unrealistic thermodynamic profiles develop, and the timing of resolved convection is severely delayed.

The air detrained by the parameterized convection may produce mesoscale cloudy regions, which are treated with the explicit moisture scheme acting on grid-scale averaged cloud. As explained in the Introduction, tropical mesoscale clouds are not just debris from updrafts, but have their own dynamics and thermodynamics leading to mesoscale ascent and rain production. It is for this reason that the explicit moisture scheme is necessary.

For this study an ice-phase parameterization and radiative transfer scheme have been added to the model.

3. Ice phase parameterization

a. Method

In a mesoscale model, where there is a necessary scale separation between convective scale and mesoscale because of the grid resolution, it is also possible to separate ice phase processes into two corresponding scales and thus, as will be seen, to simplify adding a resolved-scale ice phase parameterization to the model.

The basis of this separation is the general observation by Churchill and Houze (1984a) from WMONEX aircraft data that there is little supercooled cloud water in mesoscale cloudy regions away from convective updrafts, and, as pointed out by Rutledge (1986), GATE tropical anvil clouds are subsaturated with respect to water since they are nearer ice saturation. In fact, water droplets tend not to survive at subfreezing temperatures in the presence of ice particles because the latter consume the water vapor, and the water droplets evaporate (the Bergeron–Findeisen process). It will be seen later that depositional growth processes, even for small amounts of ice particles, are sufficiently rapid to prevent the formation of water droplets in air ascending at rates of up to several tens of centimeters per second.

The lack of water droplets in mesoscale clouds simplifies parameterization by making it possible to neglect several primary and secondary nucleation processes and to use two ice categories, ice crystals and snow aggregates, instead of the three that are normally employed in cloud models (e.g., by Lin et al. 1983). The third category is graupel or hail and represents ice particles that are heavily rimed and dense due to mixed phase growth, especially through the accretion of supercooled water droplets. WMONEX mesoscale clouds show almost no evidence of riming except in the vicinity of convective or recently convective regions. The denser rimed particles are implicitly treated in the convective parameterization scheme where much of the convective-scale rain may originate from such particles. The explicit moisture scheme described in this section is similar to that of Rutledge and Hobbs (1983) in their kinematic modeling study of warm frontal rainbands, another system where the scheme is appropriate because of the lack of convective updraft cores.

Another simplifying assumption that helps in modeling the mesoscale ice phase is that melting takes place within one model level (50 hPa) of the freezing level. That is, the cloud ice and snow melt immediately on descending through the 0°C level. This assumption is good for slowly falling particles such as snow aggregates but would not have held for heavily rimed and denser particles that may fall several kilometers while melting.

The two assumptions of no supercooled cloud or rain and no "superwarmed" snow or ice crystals between them allow for a computationally efficient means of storing snow/rain in one array and cloud/ice in another, since there is no ambiguity as to which type is present in a grid box; this being determined by the temperature relative to 0°C.

Supersaturation with respect to water is very limited, even in strong updrafts, because of the rapidity of water condensation processes. In contrast, ice processes are often slow because of the comparatively limited number of nuclei; supersaturation of water vapor with respect to ice can be around 10 percent or more. The relative rates of water and ice processes are a necessary part of a realistic moisture scheme and are important to mesoscale cloud systems, as will be demonstrated later.

The box diagram (Fig. 1) shows the processes included in the mesoscale explicit moisture scheme. The boxes represent the various moisture categories, and the lines linking them are labeled with the processes that allow transition from one category to another. The details are given in appendix B, but the scheme follows closely that used by Rutledge and Hobbs (1983) and Lin et al. (1983).

Of the assumptions, the least certain is the number concentration of ice crystals, which is strongly dependent on the temperature, increasing by approximately a factor of 400 for each 10 degree drop. The assumed concentration affects the rate of initiation of ice crystals and their growth rates. However, below about −30°C, the exact number density no longer matters because both these processes become essentially instantaneous on the model time resolution of 10 seconds. Also, above temperatures of −20°C, the ice converts rapidly to snow, which has its own number density from the Marshall–Palmer distribution. This will be shown in

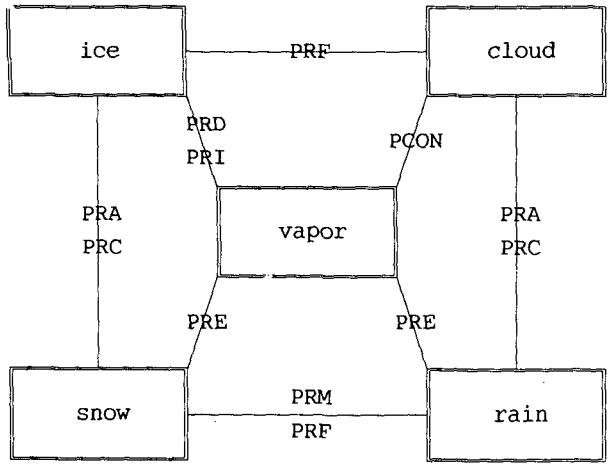

FIG. 1. Box diagram illustrating the processes in the moisture scheme for ice (crystals), cloud (liquid), snow and rain. PCON, condensation/evaporation of cloud; PRA, accretion; PRC, conversion; PRD, deposition onto ice crystals; PRE, evaporation for rain and deposition/sublimation for snow; PRF, melting/freezing due to advection; PRI, initiation of ice crystals; and PRM, melting of snow due to fall.

section 3b where the ice phase parameterization is tested in a simple one-dimensional model.

b. Test of ice phase parameterization

Before putting the scheme into the full mesoscale model, it is worth testing it under simple conditions to determine which of the parameterized processes prevail in a typical situation. The model for this test was one-dimensional with no vertical or horizontal advection. Only height variation was allowed, and the sounding used was that of the WMONEX case studied with the mesoscale model. The initial conditions were chosen to represent a possible updraft outflow. However, only a thick layer of ice crystals was specified at the initial time with a content of 0.5 g kg^{-1}. The atmosphere was saturated with respect to water in the same layer (50 hPa–550 hPa) as would be consistent with the air leaving a sufficiently rapid updraft. The model was run for 30 minutes with only the explicit moisture processes acting, i.e., no dynamical feedback to the heating was allowed for in this one-dimensional test.

These initial conditions represent a thermodynamically unbalanced state because the saturated vapor pressure over ice is significantly less than that over water. Hence, water saturated conditions are supersaturated with respect to ice. Typical degrees of supersaturation are 10% at −10°C to 50% at −40°C, so the initial conditions are favorable for crystal growth.

The results of this test show that there are two distinct regimes of behavior in the ice parameterization scheme. Above the 300 hPa level (−25°C), there is rapid adjustment to ice saturation, while below about 350 hPa (−20°C), even after 30 minutes, equilibrium still has not been reached. The ice and snow concentrations and process rates at 30 minutes are shown in Fig. 2.

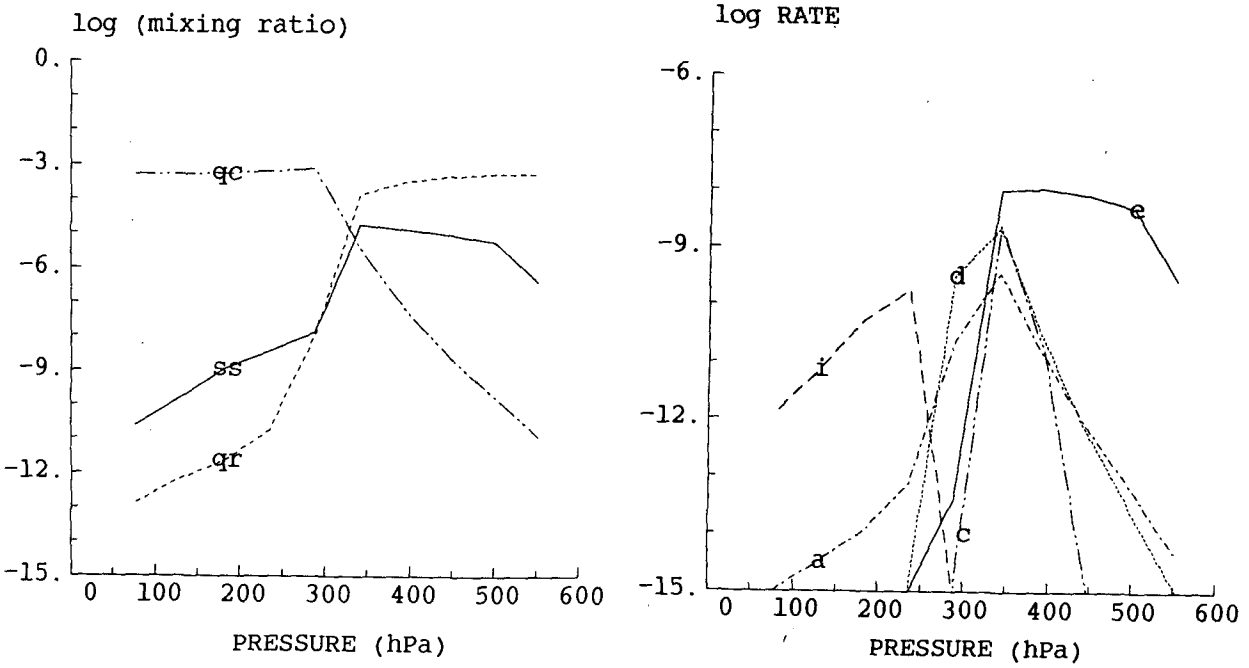

FIG. 2. (a) Snow and ice content (dashed) and supersaturation and ($\log_{10}$[kg kg^{-1}]) (b) Process rates ($\log_{10}$[kg kg^{-1} s^{-1}]) versus pressure (hPa) in ice-phase sensitivity test. Curves are labeled c, conversion; a, accretion; i, initiation; d, ice deposition; e, snow deposition; qc, ice; qr, snow; and ss, ice supersaturation.

The primary reason for this sharp separation of regimes with temperature is the number density of ice nuclei assumed in the scheme. At low temperatures, ice crystals exist in large numbers and this has two consequences.

First, the deposition rate, consuming water vapor, is much faster for a large number of small crystals than for an equal mass content of fewer larger ones. Second, the individual growth rate of a crystal is slower when there is a high number density, and hence it is almost impossible to reach such a size that the fall speed becomes significant. Thus, at 30 minutes the ice regime is at ice saturation and in equilibrium, but at lower levels the snow regime is still supersaturated and deposition still occurring. Figure 2 shows that between these regime layers is a small transition layer where deposition onto ice crystals is balanced by their growth rate into snow (precipitating ice). Accretion is generally a secondary process by 30 minutes because the presence of ice crystals and snow are almost mutually exclusive.

High number densities at low temperatures are responsible for preventing large quantities of ice from reaching a precipitable size and, in a sense, trapping it at upper levels. It is clearly important to have good data on ice crystal number densities to help parameterize this quantity with more certainty, as it directly affects the depth of the layer of mesoscale precipitation development.

As well as precipitation production, the ice phase processes described above have the important effect on mesoscale behavior of latent heating. Figure 3 shows the amount of relative temperature change, $\Delta T/T$, that will occur for a parcel as it goes from water saturation to an exact ice saturation that represents thermodynamic equilibrium. The maximum for a tropical sounding is larger than that for the standard midlatitude sounding (shown for comparison) and corresponds to a temperature change of about 0.7°C at about the 255 K level (350 hPa). This may not seem significant, but when it is considered that the updraft outflow is close to being moist-adiabatically stratified, small systematic changes in temperature may lead to a large dynamical response. For instance, if the atmosphere has a temperature lapse rate 10% more stable than wet-adiabatic, a 0.7°C temperature increase can cause an ascent on the order of one kilometer, because warm air tends to rise to its level of zero buoyancy if Coriolis effects can be neglected. This is especialy true in the tropics where the scale of convection is less than the Rossby radius; however, it may not apply to equally large midlatitude convective systems where a thermal-wind response can balance the temperature gradient more quickly so that the full potential ascent might not be realized.

The latent heating is due entirely to deposition processes in ice-supersaturated conditions, i.e. $Q = L_s(\mathrm{PRD} + \mathrm{PRE})$ [see appendix B] in the thermodynamic equation for potential temperature, θ:

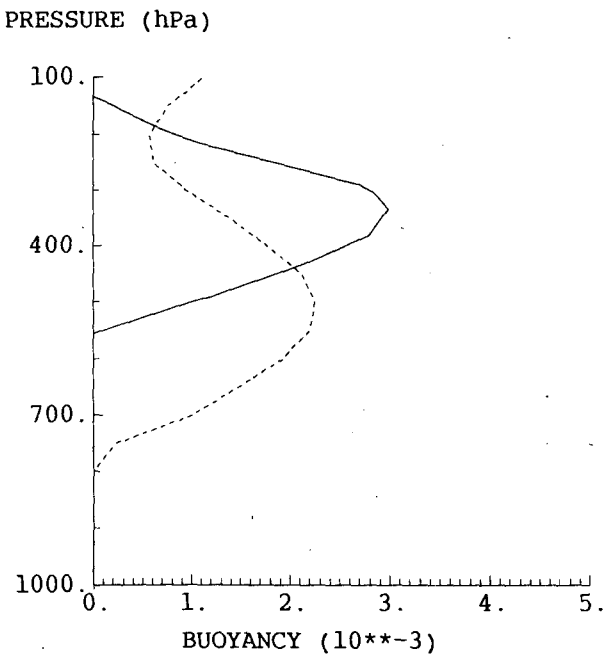

FIG. 3. Buoyancy change ($\Delta T/T$) on transition from water saturation to ice saturation as a function of pressure for WMONEX (solid) and standard midlatitude atmosphere (dashed) soundings. Vertical axis: pressure (hPa).

$$\frac{\partial \theta}{\partial t} = -w\frac{\partial \theta}{\partial z} + \frac{L_s}{c_p \pi}(\mathrm{PRD} + \mathrm{PRE}) \qquad (1)$$

where $\pi = T/\theta$. On average, advection and heating nearly cancel to leave a comparatively small local tendency. Thus mesoscale ascent and latent heating are closely correlated.

If one considers that this stratiform cloud originates as an updraft outflow with a given horizontal motion away from the updraft, the horizontal scale of the ascent is largely determined by the time scale over which the heating occurs. This in turn depends upon the deposition rates (PRD and PRE, see appendix B) of the ice or snow particles. Rapid deposition, such as that in the presence of many small ice crystals, has time scales of a few seconds to a minute and would therefore be expected to lead to ascent over a small horizontal scale near the water-saturated updrafts, essentially being indistinguishable from the updrafts themselves. However, slow deposition, such as occurs in snow-dominated regions, may act to initiate a broader scale ascent. Note that the one-dimensional model does not allow ascent, but once initiated in a cloud, there would be a dynamical feedback whereby ascent produces vertical advection of water vapor that itself would counter the depletion caused by deposition.

Consider the major terms in the water vapor equation, where vertical advection is a source and deposition is a sink in ice-supersaturated conditions,

$$\frac{\partial q_v}{\partial t} = -w\frac{\partial q_v}{\partial z} - \mathrm{PRE}(q_v, q_r, p, T), \qquad (2)$$

where PRE is the snow deposition rate that is proportional to ice supersaturation [e.g., see Eq. (B14) in appendix B]. If the vertical advection is stronger than deposition, a layer will remain at water saturation, as is the case in buoyant convective updrafts.

One can estimate a minimum value of w for which water saturation can be maintained. Figure 4 shows this limiting velocity, $w_{\mathrm{lim}'}$, for typical snow concentrations, q_r, and at various heights in the WMONEX sounding. It is calculated from (2) with the left-hand side set to zero, where $w = w_{\mathrm{lim}'}$, the snow deposition rate, PRE, is calculated at water saturation, and the mean vertical moisture gradient, $\partial q_v/\partial z$, is well approximated by the saturated vapor content gradient because there are no large variations in humidity. Lesser values of w lead to proportionately smaller degrees of ice supersaturation. Ice crystals in cirrus clouds have a much greater deposition rate and hence would required greater vertical velocities to maintain water saturation. However, in the snow-only regime ascent rates around a few tens of centimeters per second can result in a highly supersaturated state.

The important point about w_{lim} is that snow deposition can only release the additional latent heat associated with the transition from water to ice saturation (seen from Fig. 3) through slow ascent rates compared to these limiting values shown in Fig. 4 (because at greater ascent rates water saturation persists); consequently, long time scales are required. In fact, to release all of the available latent heat, the ascent rate would eventually have to tend to zero because the deposition rate decreases in proportion to ice supersaturation, so one envisages a gradually decaying ascent in the mesoscale updraft as it is advected further from the convective source region and as the supersaturation decreases. Considering that an air parcel may have to rise a kilometer (as seen earlier) to reach its final buoyant equilibrium level and that, if $w_{\mathrm{lim}} = 40$ cm s^{-1} its ascent rate may average 20 cm s^{-1}, a typical time scale would be 5000 s. Eventually the parcel will be both at thermodynamic and buoyant equilibrium and so would have no further tendency to warm or rise.

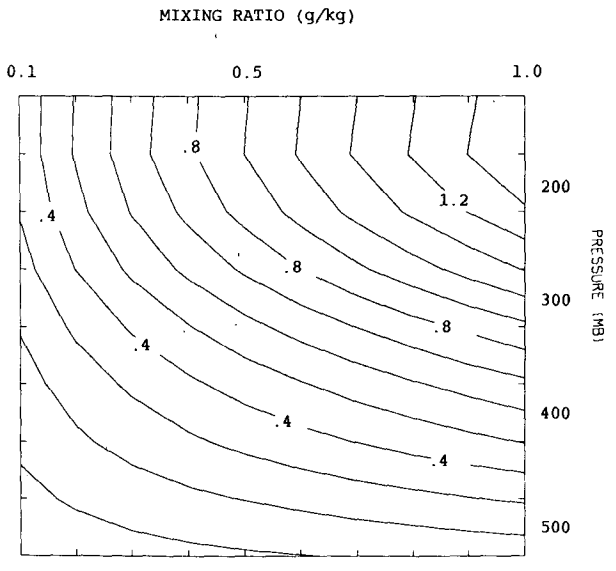

FIG. 4. Vertical velocity (m s^{-1}) above which water saturation is expected for varying snow contents (g kg^{-1}, horizontal axis) and pressures (hPa), vertical, temperatures from WMONEX sounding.

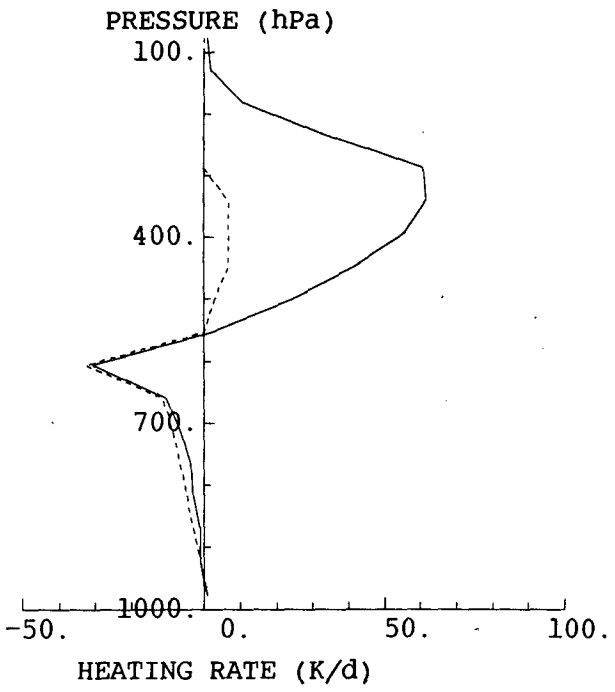

FIG. 5. Heating profile (K d^{-1}) in ice sensitivity test averaged over 0–900 s (solid) and averaged from 900–1800 s (dashed). Vertical axis: pressure (hPa).

Snow depositional warming can be regarded as the thermodynamical negative of rain evaporative cooling and, as just shown, can drive mesoscale motion given an initial supersaturated state such as that provided by convective updraft outflows, though particle drag opposes rather than reinforces it. A full mesoscale model is needed to investigate this complex interaction between mesoscale motion and thermodynamic processes.

Figure 5 shows the heating profile associated with ice phase processes in the test simulation both from 0–15 minutes and averaged from 15–30 minutes. The strong time dependence is demonstrated by the difference between the two curves. The heating maximum generally shifts downward from around 300 hPa to 400 hPa and decreases in magnitude from almost 60 K d^{-1} to less than 10 K d^{-1}. Most of the temperature change

occurs within the first 5 minutes of the test's start as is consistent with the presence of small ice crystals. This is followed by a gradual decay in the warming rate lower down. The slow depositional processes associated with snow act in a layer near the maximum available heat (Fig. 3) and therefore, from the discussion earlier in this section, can initiate significant mesoscale ascent. Above 325 hPa, although a comparable amount of heat is released to that below 325 hPa, it is on a time scale too short to act far from an updraft. Figure 5 also shows the effects below the cloud of melting and evaporation that are equally important in driving subcloud motion. The cooling provided by these probably would act to maintain mesoscale subsidence. Because of the stability of the lower troposphere, moist thermodynamic processes play an important role in allowing any significant vertical motion, and this will be investigated further in the mesoscale model.

4. Radiative transfer parameterization

a. Method

The radiative transfer scheme acts on the model's vertical resolution, about 50 hPa, and is used to calculate the upward and downward fluxes from the effective emissivity for longwave radiation and the downward flux of shortwave radiation from scattering and absorption. The net flux at the ground is included in the energy budget for the land surface. The radiative calculations are carried out and the heating rates updated at 20 minute intervals since it is a slowly varying field and computationally costly.

The vertical resolution is coarse for a radiative scheme, particularly within cloud layers where the effective radiative path-length is overestimated due to the model's finite layer depth. This may lead to spurious warming of a few tenths to 1 degree per day within such layers and so is not considered a serious drawback.

1) LONGWAVE SCHEME

In clear air, the temperature-dependent emissivity functions calculated by Rodgers (1967) are used. These are based on a fit to accurately calculated fluxes for the water vapor absorption bands in a range of clear-air atmospheric conditions from polar to tropical. Although the use of downward clear-air emissivity is not as accurate for conditions below a cloud ceiling, the error of up to 20 W m^{-2} in flux is acceptable.

Clouds are assumed to be horizontally uniform on the resolved scale, 10 km, and the liquid water, ice and water vapor paths are derived from model data. Stephens' (1978) scheme is employed for cloud water.

As precipitating particles are larger than ice crystals and cloud droplets, their mass absorption coefficients are smaller. The absorption length scale varies from 60 meters for 0.1 g m^{-3} of cloud water to 3000 meters for 0.1 g m^{-3} of rain water.

The cloud and precipitating particles are incorporated as "grey bodies" (no wavelength preference) by a similar overlap technique to that used for the carbon dioxide band. More details are given in appendix C.

2) SHORTWAVE SCHEME

Solar radiation includes the effects of the reflected or backscattered component. However, it is assumed that the scattered beam does not interact further with the atmosphere as this is a second order effect. Clear-air and cloud scattering are included. Clear-air absorption arises primarily from water vapor.

All cloud and precipitation is treated as one type of cloud, and the albedo and absorption are based on the theoretical values given by Stephens (1978). The initial convective development occurs at midnight, and therefore shortwave effects only become important in the later mature to decay stages. For thick clouds and low zenith angles, absorption can reach 15% mostly in the upper layers of the cloud, and thus a significant contribution to cloud heating may occur. This and longwave effects will be tested in section 4b. Details of the shortwave scheme are given in appendix C.

b. Tests of radiative scheme

In this section the radiative schemes outlined above are used to calculate the heating profile for various cloud tops and bases. The scheme is run one-dimensionally on a specified cloud to provide the heating rates. The clouds considered here are sufficiently thick to be black with respect to longwave radiation, hence cloud top and cloud base act independently, and the heating rates will be expressed for a 50 hPa thick layer including the cloud boundary.

Figure 6 shows the effect of a cloud layer on the radiative heating profile as the height of the cloud top and cloud base are varied in a WMONEX sounding. Curve (a) shows the effect of varying the height of cloud top on longwave radiative cooling at that level. The greatest radiative cooling occurs for tops around 350 hPa (22 K d^{-1}). Above this the cooling rate is reduced by lower cloud top temperatures and hence reduced upward radiative flux. For tops below about 400 hPa, the cooling is lessened by the blanketing effect of clear-air water vapor absorption above the cloud, which is important in tropical atmospheres.

Curve (b) shows the heating at cloud base as its height is varied. Again, the water vapor content of clear air below the cloud is sufficient to reduce the radiative effect of the lower levels at the cloud base except for bases above 400 hPa where the heating rate increases up to 20 K d^{-1} (at 150 hPa). These heating and cooling rates, as suggested by Webster and Stephens (1980), may be comparable in magnitude with those of melting

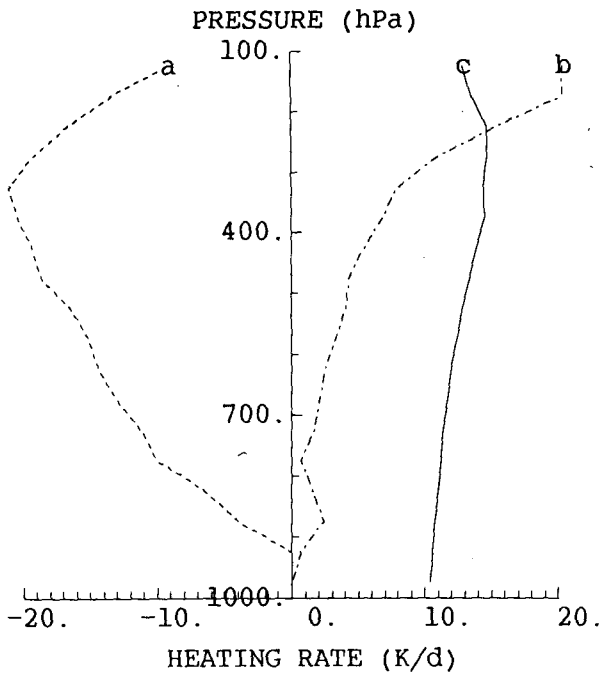

FIG. 6. Heating profile (K d^{-1}) in radiation sensitivity test. Maximum longwave cooling for varying cloud tops (dashed), warming for varying cloud base heights (dot–dash) and shortwave warming (zenith angle = 45°) for varying cloud top heights (solid). Vertical axis is pressure (hPa) of cloud top/base.

at cloud base and other latent heating processes in mesoscale clouds.

Cloud top heating for shortwave radiation is shown by curve (c) as a function of cloud top height. For solar radiation, clear-air absorption and scattering have little effect, but the absorption in the cloud is sensitive to cloud water content and the solar zenith angle. The results plotted are for a zenith angle of 45° and a liquid content of 0.1 g kg^{-1}, giving a heating rate of around 13 K d^{-1}. For 1 g kg^{-1}, this increases to 18 K d^{-1}, and for 0° zenith angle (0.1 g kg^{-1}), it is 20 K d^{-1}. Shortwave heating also extends further into the cloud than longwave cooling and may significantly offset its effects at cloud top during the day, leading to a net radiative heating in the cloud.

Another radiative effect, which can only be studied in a two- or three-dimensional model, is that of longwave cooling in the clear regions relative to the cloudy region that may enhance cloud activity. This will be investigated later.

5. Cumulus parameterization

With a horizontal resolution of 10 km it is essential to represent subgrid-scale vertical transports by updrafts and downdrafts because resolved scales of motion cannot transport boundary layer air into the upper troposphere, nor midtropospheric air to the surface realistically. The convective parameterization also must maintain realistic thermodynamic properties in its updraft and downdraft detrained air because these form the upper level cloud deck and the surface cold pool; both are features that spread to resolved scales. For these reasons, the cumulus parameterization scheme of Frank and Cohen (1987) was chosen. This incorporates a one-dimensional cloud model to predict updraft and downdraft properties. A few minor changes to the scheme have been made for this study.

The basis of the scheme is that the updraft mass flux depends on the time-averaged mass convergence at a grid point in the ten minutes prior to the updraft's initiation. If the time averaged horizontal convergence exceeds a critical value in the lowest 50 hPa, typically $2 \times 10^{-5}\ s^{-1}$, an updraft is formed with twice the mean vertical mass flux at cloud-base. Updraft properties are predicted from a one-dimensional cloud model that includes entrainment and detrainment. The lateral entrainment rate, ϵ, is specified according to the initial mass flux, being relatively greater for smaller mass fluxes and detrainment, δ, is set at a fraction, α (=0.5), of entrainment.

The one-dimensional cloud model is applied at each convective grid point to determine cloud top and heat, water and momentum transports. Differences from Frank and Cohen's cloud model adopted for this study include increasing maximum updraft cloud water from 0.5 to 2.5 g kg^{-1} representing a different equilibrium between condensation and precipitation production. Also, for simplicity, a constant (rather than height-dependent) fraction of convective precipitation (20%) goes into mesoscale precipitation. The convective downdraft is driven by evaporation of the remaining convective rainfall into the environment and is saturated except near the surface. Its entrainment and detrainment rates are set at about $(250\ hPa)^{-1}$ and $(330\ hPa)^{-1}$. The downdraft is not active until a period of one cloud lifetime, τ, has elapsed from the parent updraft's initialization and lasts for one cloud lifetime. This period, typically 15 to 25 minutes in Frank and Cohen's scheme, was the subject of sensitivity studies (discussed later) and it was found that 40 minutes produced a more realistic convective growth rate for the present study.

Compensating motion is included that is primarily subsident in response to the updrafts. Thus, the net mass flux introduced in a convective grid column by Frank and Cohen's scheme is zero, it just redistributes heat and moisture by entrainment, detrainment and compensating motion. However, the net effect is generally heating, mostly from subsidence, forcing the mesoscale model to respond with an upward vertical mass flux that opposes the heating through adiabatic cooling.

An important point to note is that, with a 10 km resolution, the model is effectively parameterizing

convection on the scale of one or two updrafts per grid column unlike most cumulus schemes where whole cloud populations are represented in a grid column. Here, the cloud population is generated at separate grid points by varying mass fluxes producing various entrainment rates and hence cloud top heights.

It is probable that, for strong midlatitude or land-based daytime storms, a 10 km resolution is too fine for a hydrostatic model since convective heating will be much larger than it is for the tropical oceanic cases considered here. This was demonstrated by a test simulation where the heating rate was doubled from that predicted by the model (which itself is up to 500 K d^{-1}). It was found that the resolved-scale motion was unable to keep pace with the heating, allowing large positive temperature deviations to develop in the convective area and strongly amplifying the surface pressure perturbations. This unrealistic behavior probably results because the grid resolution and hydrostatic approximation were insufficient to produce the vertical accelerations necessary to respond to heating at this rate. In all the simulations presented later, the surface pressure perturbation was always small (of order 1 mb), as were tropospheric temperature deviations, indicating that the hydrostatic approximation on the resolved scale was adequate for these systems; however, there is a definite limit on the strength of convection that can be represented in such a model. The limit, for a 10 km grid, seems to occur for resolved vertical motion of moderate strengths; 1 m s^{-1} is stable, and 2 m s^{-1} is unstable.

The cumulus parameterization has to interface consistently with the explicit moisture scheme. Updrafts in the one-dimensional cloud model are assumed unfrozen until they reach −25°C, above which freezing contributes to the updrafts' latent heating. Thus, between 0° and −25°C the detrained water has to be evaporated or frozen to be consistent with the mesoscale moisture assumptions described earlier. Hence, the detrained cloud water is evaporated, and the precipitation is frozen in the mesoscale environment. Above the −25°C level all the detrained cloud and precipitation is already frozen, so no adjustment is required. Parameterized convective precipitation melts at 0°C. Rutledge and Houze (1987) found that their kinematic model was quite insensitive to ice and supercooled cloud water, which they specify at a steady convective inflow boundary, so neglect of these is unlikely to affect the behavior of the mesoscale clouds.

6. Observations and model initialization

The case chosen for this study was that of 16–17 December 1978, which exhibited many features typical of convective development observed during WMONEX, particularly during December. Satellite and radar data show this case to be a good example of those described by the conceptual model of Houze et al. (1981) and the study of Johnson and Kriete (1982). Figure 7 depicts the radar sequence from Bintulu on the coast of Borneo of this case at three-hourly intervals from 1800 UTC 16 December to 0300 UTC 17 December 1978 corresponding to the development until decay of the convection. By the end of this sequence, the system is moving out of radar range and is probably more active than shown. The overall offshore propagation is apparent, and the model domain represents a northwest–southeast section in this direction of general motion perpendicular to the coast.

The ship *Akademik Korolev,* stationed about 150 km offshore, provided the sounding used in the model. The wind and thermodynamic profiles (Fig. 8) at 1200 UTC 16 December were taken as initial conditions, representing a time about 4 hours prior to the first convective clouds near the coastline. The local solar time (LST) is 7.5 hours later than UTC.

As is typical in the tropics, the thermodynamic sounding varies little from day to day and that of 1200 UTC 16 December is close to the mean 1200 UTC sounding of the week prior but about 1°C cooler in the lower troposphere. The wind profile is also similar to the mean. The hourly surface data at *Akademik Korolev* shows strong cooling from deep convection at 2300 UTC (0630 LST), compared to typically 0300 UTC (1030 LST) earlier in the week. This demonstrates that there is a range of variability between individual WMONEX days. As stated by Houze et al. (1981), the convection first develops around 0000–0200 LST near the coastline and so takes about 6 hours to reach the ship.

Another ship around 500 km offshore, *Priliv,* shows soundings that are much less favorable for convection. The surface layer is drier and cooler and the sea temperature is almost 2°C cooler than at *Akademik Korolev.* It is likely that the decay of convection largely resulted from its propagating into these less favorable conditions that persisted further offshore. The gradient of thermodynamic conditions was probably maintained by mean advection from the northeast parallel to the coast, a process not included in the model, which is aligned in the plane perpendicular to this flow. However, the sea surface temperature gradient was included so that the boundary layer might reach equilibrium with the cooler conditions observed further offshore.

The initial atmospheric sounding was taken to be horizontally uniform over a 700 km domain that includes 200 km over land, 500 km over ocean, and is aligned northwest–southeast. The assumption of equal temperatures over the land and sea surfaces was considered consistent with early evening conditions. There is also simplified terrain up to 500 m, starting 50 km inland, to represent that on Borneo. The sea temperature was specified and kept constant throughout the simulation. The land surface temperature was initially

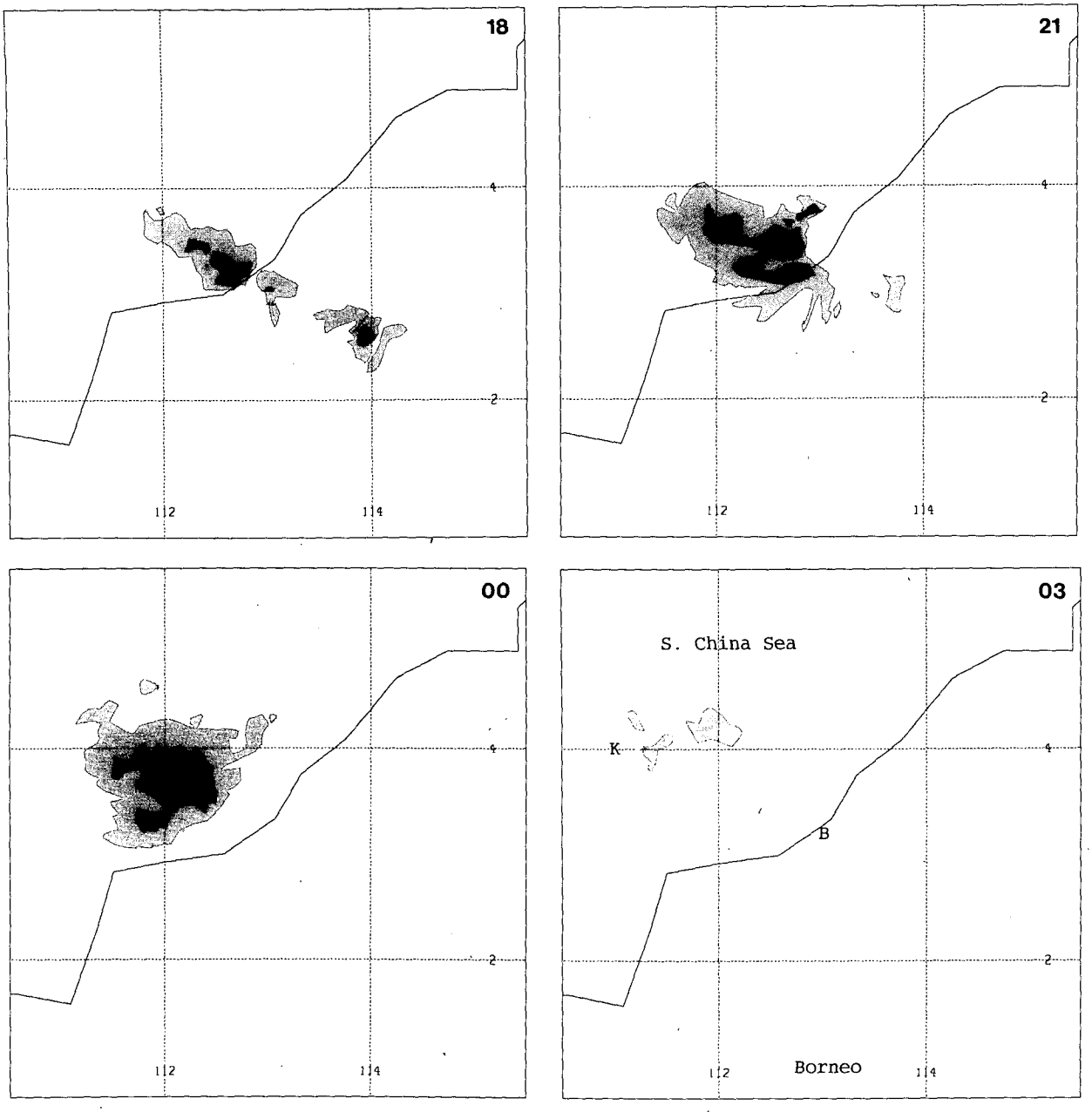

FIG. 7. Radar images (1.5° elevation) for 1800, 2100, 0000, and 0300 UTC 16–17 December at Bintulu. Contours at 10, 30, 40 dbZ. B and K on 0300 plot mark positions of Bintulu and ship *Akademik Korolev*. Latitude (°N) and longitude (°E) lines marked.

set to 3°C below the lowest level (250 m) potential temperature, also consistent with conditions expected around 1930 LST, and the subsurface temperature, required for the slab surface parameterization, was set equal to the surface temperature. These temperatures were estimated by running a slab model alone for a few days, until an equilibrium diurnal cycle was reached, with a parameterized atmospheric layer and radiative flux to help determine appropriate surface and subsurface temperatures for the initial time of the simulation.

The model includes a Coriolis force, so it is necessary to impose a thermal wind balance at the initial time to prevent turning of the mean wind from occurring. This balance is achieved by ensuring that the component of the wind perpendicular to the domain, v, is vertically unsheared, consistent with the domain's initial zero horizontal temperature gradient. The wind

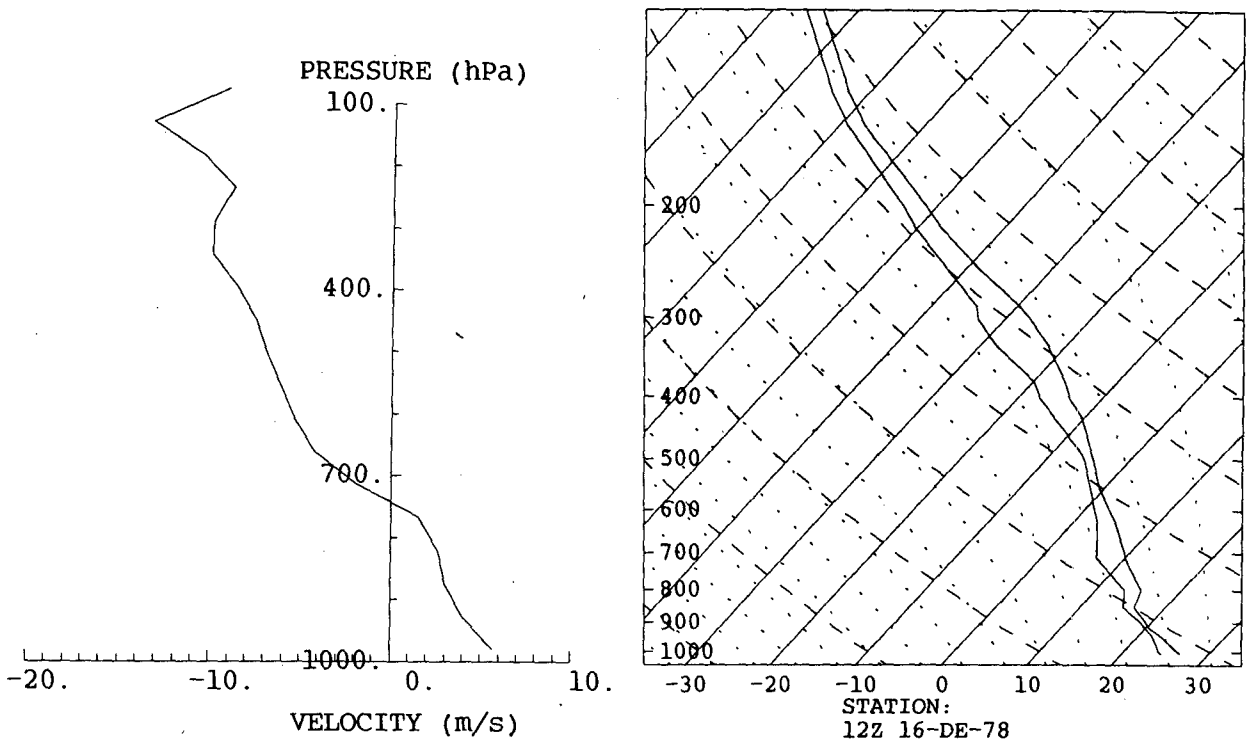

FIG. 8. (a) Component of wind perpendicular to coast and in model's domain plane (m s^{-1}) from ship *Akademik Korolev* at 1200 UTC 16 December. Positive is towards southeast (onshore component). Vertical axis: pressure (hPa). (b) Thermodynamic sounding (skew$T$–log$p$) from same time and position used to initialize the model.

component in the domain, u, is taken to be geostrophically balanced initially. In the lowest 100 hPa of the domain a frictional rotation is added having been estimated from a simple analytic one-layer model incorporating the mesoscale model's strength of surface friction. Thus, the lowest level winds have initial ageostrophic components to balance the friction. The geostrophic component of the wind is kept constant throughout the simulation.

Because of the presence of terrain, it is preferable to speed up the wind from rest over the first 1000 s. This is necessary to prevent the production of unrealistic waves that would result from convergence in the initial horizontally uniform flow as it encounters terrain. During this short speed-up phase, the Coriolis force is switched off.

7. Model results

a. Development stage

The model's initial conditions include nothing that will initiate convection immediately since there is no convergence in the wind at the surface. The flow over the terrain is smooth because of the slow speed-up procedure described in section 6. There are also no initial horizontal temperature gradients that can initiate convection, but the atmosphere is conditionally unstable.

During the first few hours of the simulation, the air temperature above the land cools relative to that over the ocean. This happens because, although nocturnal radiative cooling affects both regions of atmosphere equally, the ocean's upward heat flux (3–4 W m^{-2}) tends to sustain the boundary layer temperature more than does the cold land surface where the heat flux is negative (−20 W m^{-2}). This causes the development of a small horizontal air temperature gradient near the coastline despite the onshore advection of warmer air by a 5 m s^{-1} wind in the lowest 500 m that tends to smooth out the temperature gradient.

After 1.5 hours (2100 LST) small clouds with tops around 3–4 km develop just offshore. These result from the small convergence at the coast associated with the temperature gradient although no land breeze, in the strict sense of an offshore-directed flow, has developed. The convergence results more from the effect of the mean onshore flow meeting denser air over the land. The cumulus parameterization scheme produces clouds that have low mass flux and a consequently high entrainment rate, thus the tops are initially low and precipitation is weak.

Clouds with tops of 5+ km do not develop until 3 hours (2230 LST), and are associated with a weak vertical motion seen in Fig. 9a while the cloud population extends away from the coast, The greatest vertical mo-

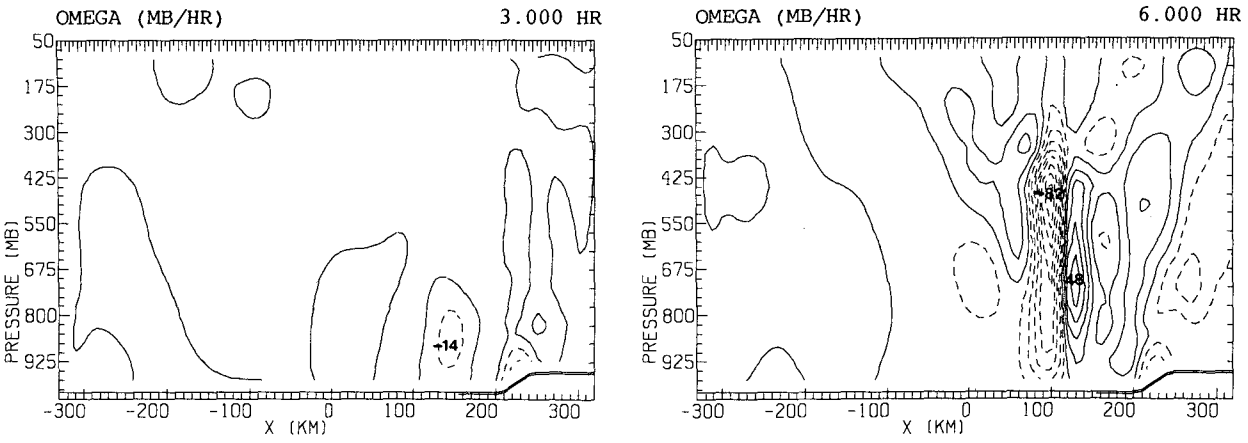

FIG. 9. (a) Three hour vertical motion, (b) 6 h vertical motion. Whole domain. Contour interval 10 hPa h^{-1}. Note terrain and land (indicated by double surface line).

tion at this stage is related to the low-level ascent over the topography. The development of vertical motion between 3 and 6 hours (Figs. 9a and 9b) indicates that convection has intensified strongly and that it has also started to propagate. The convergence forcing mechanism at this stage is not solely the land cooling but also the effect of convective and mesoscale downdrafts, which provide a faster and greater drop in temperature. It appears that weak convergence occurs ahead (seaward) of the cool air as a result of long deep gravity waves that form in the convective region. This produces small clouds ahead of the system that, therefore, propagates seaward. However, the newly formed clouds do not reach significant strength until the convergence associated with the cold air pool overtakes them. The presence of both gravity-wave forced and temperature-gradient forced convergence in producing clouds is important as it is a combination of these that determines the propagation speed of the system. This point will be discussed further in the cloud parameterization sensitivity studies (section 8).

The development time scale generally agrees with that of the observed initial clouds and their positioning just offshore. Also the Houze et al. (1981) low-level wind (0–1500 m) analysis at Bintulu (on the coast) shows that in the average WMONEX situation, the wind by 0200 LST is not yet offshore so a land breeze is not fully developed at the time of initial convection. Hence it is likely that the temperature gradient forces convergence rather than a directly opposing flow.

A sensitivity study in which the topography was removed demonstrated the importance of the sloped surface inland to the timing of development, since the convection took 3 hours longer to begin propagating, and thereafter remained 3 hours behind the simulation with topography. It appears that the topography significantly enhanced the land breeze effect.

The initial development stage ends around 6–8 hours (0130–0330 LST) when the rain area attains a steady size that varies little during the mature phase.

b. Mature stage

Between about 8 and 14 hours (0330–0930 LST) the convective area propagates at 6–7 m s^{-1} and has a constant overall structure. This consists of a convective region and a mesoscale precipitation region as seen in Fig. 10a, the former covering an area of around 50 km with intense precipitation while the latter produces rather less intense rainfall on the scale of 100 km. Unlike tropical squall lines, which are also divided in this way, the convective region is partially inside the mesoscale rain area; i.e., some mesoscale rain falls ahead of the convective clouds. This is because the system is slow moving and the upper winds overtake the cloud updrafts, having a relative forward flow compared to the system propagation. This is similar to the GATE case studied by Houze and Rappaport (1984). In most tropical squall lines the mesoscale rain is completely behind the convective region because the upper winds usually flow rearwards in the relative frame. There is a qualitative similarity between the WMONEX systems and midlatitude squall lines that exist in a strong westerly shear, but the magnitude of the shear is somewhat less for these tropical systems—being around 10–15 m s^{-1} per 10 km compared to typically 25–30 m s^{-1} per 10 km for midlatitude squall lines, and consequently the propagation speed is much less (6–7 m s^{-1} compared to 15–20 m s^{-1}).

The modeled system does not produce as much point precipitation as is observed, 40–60 mm compared to the model's 20 mm, but this may be a result of the neglected three-dimensional or larger scale effects described later. Of the rainfall at the surface about 65%

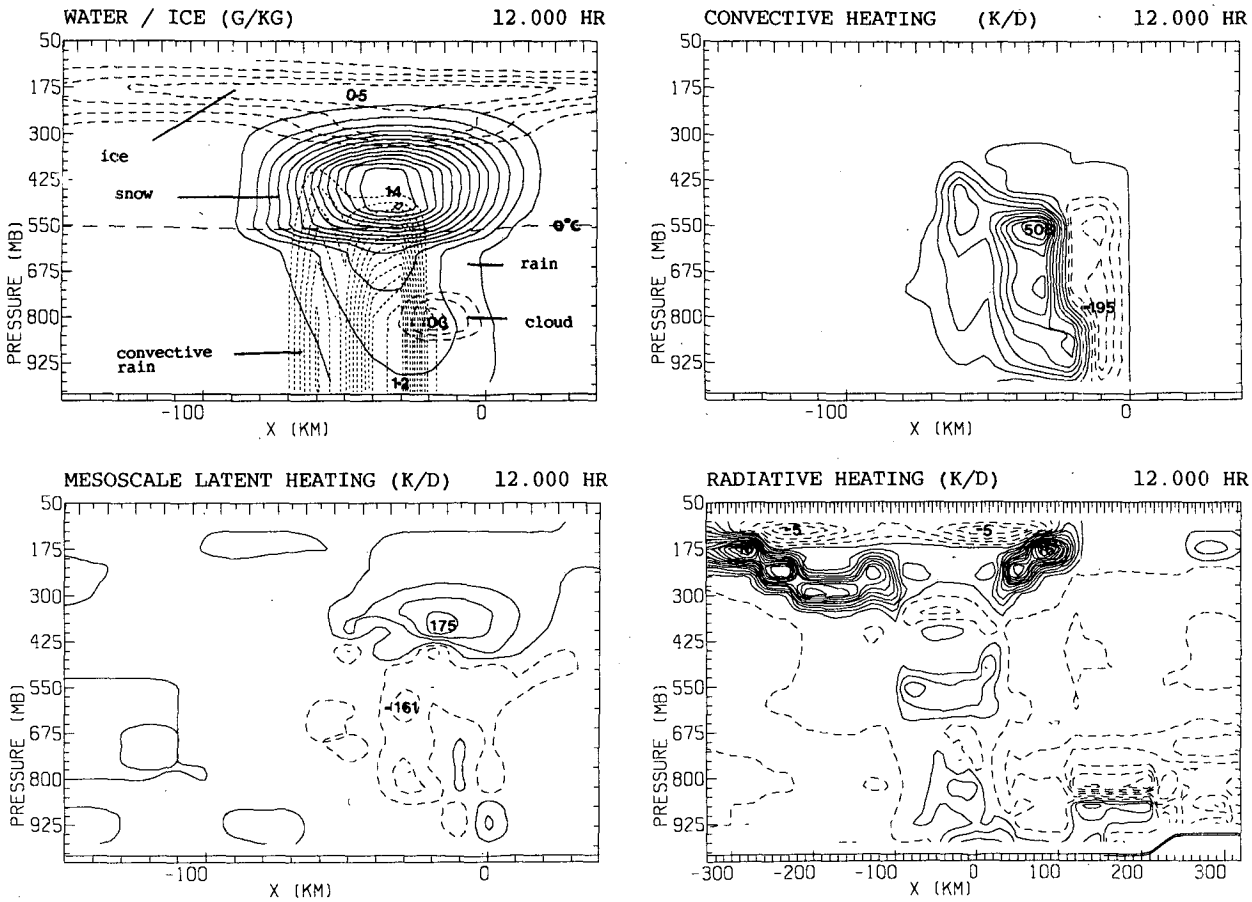

FIG. 10. (a) Cloud/ice (dashed), resolved precipitation (solid) and convective scheme's precipitation (dotted) at 12 h in a 200 km section of domain. Contour interval 0.1 g kg^{-1}. Pressure (hPa) vertical and distance (km) horizontal. (b) Convective heating, (c) resolved scale latent heating, (d) radiative heating on whole 700 km domain (exaggerated contour scale). Contours for (b) and (c) 50 K d^{-1} and for (d) 1 K d^{-1}.

is convective and 35% is mesoscale, but there is a tendency towards a higher mesoscale fraction later in the mature stage when it approaches 50%.

Associated with the system is a cirrus shield between about 100 and 250 hPa, covering an area of 500 km at 12 hours and expanding ahead of the rain area by up to 300 km where it is quite tenuous (0.02 g kg^{-1}). It has an ice content greater than 0.1 g kg^{-1} over a 340 km region, and its maximum at 12 hours is about 0.5 g kg^{-1} at and just ahead of the convective towers which are the source as seen in Fig. 10a. Below the cirrus cloud is the stratiform precipitation cloud that extends down to the melting level. The mesoscale precipitating ice (snow) content at 12 hours is greater than 0.1 g kg^{-1} in a 90 km region with a maximum of 1.4 g kg^{-1} around 450–500 hPa. On melting below 550 hPa the content drops to 0.3–0.4 g kg^{-1} consistent with the acceleration in fall speed. By the time it reaches the surface, evaporation has removed about half of the rain that existed at the melting level.

Up to 6 hours in the simulation, the subsidence is deep and is equal ahead of and behind the system suggesting that it is mostly dry compensating motion. Later (see Fig. 11a) the subsidence becomes concentrated mostly behind the active convection and in the lower troposphere. This indicates that it is driven by evaporation in the decaying convective region and the mesoscale rain area. Typical evaporative cooling rates of up to 50 K d^{-1} exist in the mesoscale rain area and melting contributes a similar amount in the 50 hPa layer around the 0°C isotherm.

Convective heating from the cumulus scheme can reach values of 300–500 K d^{-1} in an active grid column as shown in Fig. 10b. In the mature stage, the clouds detrain mostly around 400–450 hPa, but the vertical motion field (Fig. 11a) shows strong ascent even above the detrainment layer (Fig. 11b will be referred to in section 8b). As stated earlier, the ascent rate depends upon both the heating rate and the stability of the environment. Since the environment above 400 hPa is less stably stratified, ascent rates can be generated that are comparable with those produced lower down by

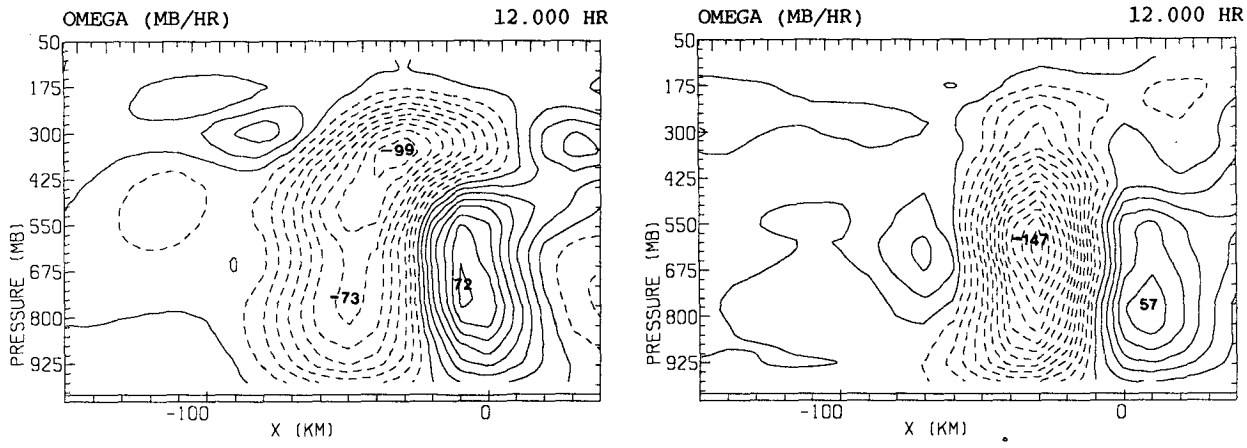

FIG. 11. Domain and axes as Fig. 10a, (a) 12 h vertical motion. (b) 12 h vertical motion in "no ice" simulation. Contour interval 10 hPa h^{-1}.

cumulus convection, by processes with smaller heating rates such as mesoscale vapor deposition onto snow or ice. In fact, the latent heating rate from deposition onto snow is the main driving mechanism for the mesoscale ascent above 400 hPa and has a strength of over 100 K d^{-1} at about 350 hPa (Fig. 10c).

Mesoscale ascent has a magnitude that varies from 50 cm s^{-1} close to the convective region to 5 cm s^{-1} about 50 km behind it. As discussed in section 3, this ascent has a long time scale and therefore a large horizontal spatial scale. It is fueled by a convective outflow supply of supersaturated (with respect to ice) water vapor containing a low number density (around 10 per liter) of hydrometeors and by its own vertical advection of water vapor; the latter being significant only because ascent occurs in the nearly saturated wet-adiabatic environment of the convective outflow layer. In a system where the convective region propagates rapidly relative to its upper outflow, such as a tropical squall line, the mesoscale ascent region would be extended further from the convective region possibly producing the long trailing stratiform cloud seen in many observational studies (e.g., see Houze and Betts 1981).

Above 300 hPa, the mesoscale ascent takes place in cloud just saturated with respect to ice because of the large number density of ice particles, as shown in section 3. This layer is likely to be ascending only because it is forced by the mesoscale ascent below since it is neither supersaturated nor warm compared to the ambient environment. Deposition onto ice occurs in this layer and provides latent heat, but this is only in response to the adiabatic cooling of forced ascent.

Thus supersaturation introduces a subtle dynamical difference in the cloud below 300 hPa that distinguishes its behavior from that above and enables it to drive mesoscale ascent. It does this because supersaturation represents a store of unreleased latent heat which, from the arguments of section 3, can only be released in slowly ascending or nonascending conditions when there is a low number density of ice particles. It will be seen in the next subsection that radiative heating has a similar but smaller effect on the upper clouds, particularly the cirrus outflow. Its contribution in the mature stage is up to 16 K d^{-1} shown in Fig. 10d.

The peak in domain-integrated precipitation content (including rain and snow) is reached at 13.5 hours (Fig. 12) after which there is a steady decline to about one-third of the peak value by 18 hours. This marks the decay stage of the system.

c. *Decay stage*

By 18 hours (1330 LST) the system has weakened considerably in terms of convective activity and me-

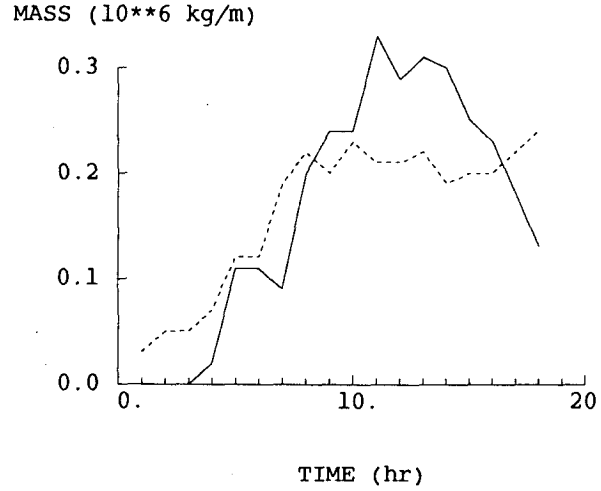

FIG. 12. Domain total precipitation mass (rain plus snow, solid) and cloud mass (ice plus water, dashed) in units of 10^6 kg m^{-1} (vertical) as a function of time (horizontal, hours).

soscale rainfall (Fig. 12). This occurs primarily because its propagation takes it into a less favorable boundary layer that results from cooler sea surface temperatures, 2°C less than at the coast. However, there is a new weak convective development at the coast starting at 14 hours that persists in that vicinity. It probably begins in response to the recovery of the surface boundary layer that results from sea-surface fluxes of heat and moisture.

On the resolved scale most of the ascent seen in Fig. 13 is associated with the low and weak convective towers and also the thick high cirrus, especially near its base at 250 hPa ($x = -250$ and $x = 0$ km). The latter ascent is clearly not due to latent heating since the cirrus cloud is not supersaturated, nor unstably stratified with respect to the ice adiabat. In fact it results from the longwave radiative heating at cloud base which is shown in Fig. 14 and has a maximum value of 24 K d^{-1}. This is more than at 12 h because of the increase in shortwave radiation. The top of the cirrus cloud has little net heating or cooling around midday because shortwave and longwave effects tend to cancel there. As was shown in section 4, infrared heating at cloud base is particularly strong for high bases with clear air below, and this is the situation here. There are only some low clouds in the lowest kilometer that have little effect on the radiative heating rate at 250 hPa. This heating leads to saturated ascent of 10–20 cm s^{-1} in 100 km long × 3 km thick layer ahead of and behind the convective region (Fig. 13). The solar angle appears crucial to this radiative forcing since, before shortwave heating becomes significant, the cirrus shows little sign of mesoscale ascent. It is only when cloud top longwave cooling is canceled in the late morning hours that ascent begins, because it is then that there is net heating in the cirrus deck compared to the ambient air at that level.

As has been emphasized before, the heating rate due

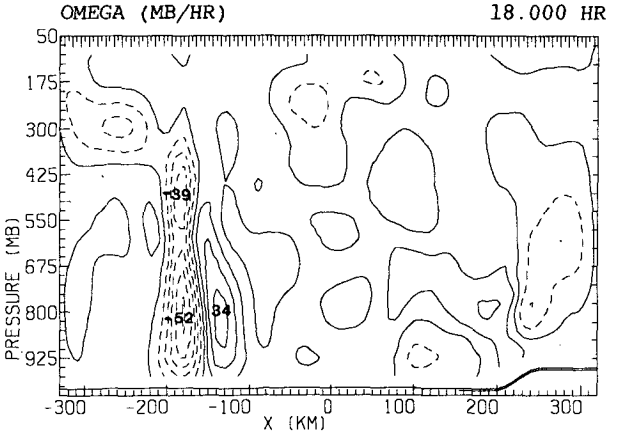

FIG. 13. Vertical motion as Fig. 11a at 18 h but showing whole domain (700 km).

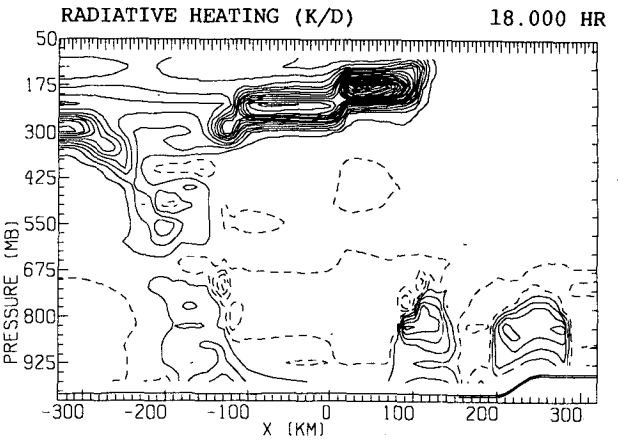

FIG. 14. Radiative heating as Fig. 10d at 18 h. Maximum value is 24 K d^{-1}.

to radiation is small (about 10–20 K d^{-1}, see Fig. 14), but the stability, taking into account ice-adiabatic processes, is also small so that comparatively large ascent rates result. The latent heat of deposition released by this saturated ascent also provides heating of around 10-15 K d^{-1}. Here the radiative heating is forcing ascent while the latent heating just maintains ice saturation.

It can be seen from Fig. 14 that radiative heating increases strongly for higher cloud bases as explained in section 4. Also note the slight differential radiative heating in the midtroposphere between the convective region and the clear region (2 K d^{-1}). It is a gradient of heating such as this that may be responsible for the diurnal modulation in the GATE region's convection as suggested by McBride and Gray (1978).

d. Average heating profile

Figure 15a shows the heating profile associated with the four main heating processes in the model. These contribute to the temperature prediction equation and can be found in Eq. (A4) in appendix A. Convective heating (C_T) is that from the cumulus parameterization scheme, mesoscale heating is the resolved-scale latent heating (Q/c_p), radiative heating (R_T) is the long- and shortwave contribution, and vertical heat flux convergence (P_T) is the subgrid-scale vertical transport, which is strong only in the surface layer. Figure 15a shows the average over the full 18 hour simulation and over the 500 km marine part of the domain. During this period there is an average rainfall of 0.5 mm h^{-1} at the surface.

It can be seen that the convective and mesoscale heating almost mirror each other in the lower and midtroposphere. The peak in mesoscale cooling around 550–600 hPa is due to the contribution of 3 K d^{-1} melting at that height while below that, evaporation of rain dominates. It is noticeable that convective heating

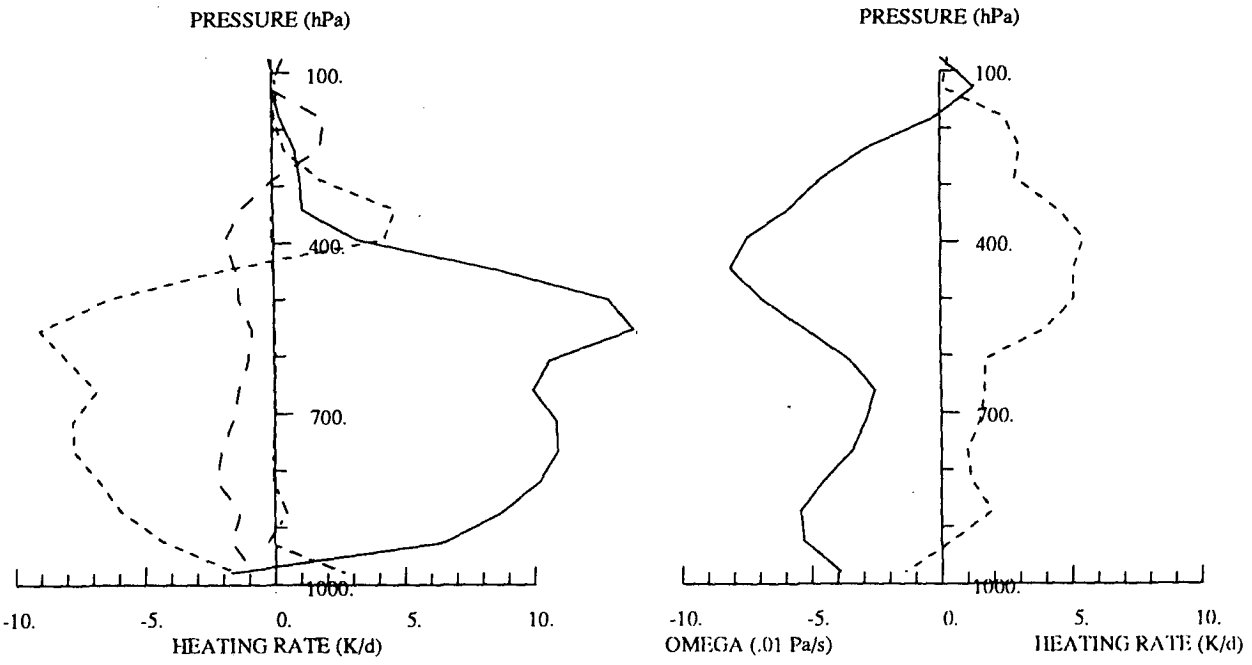

FIG. 15. (a) Heating profile averaged over 18 h and 500 km due to convective heating (solid), mesoscale latent heating (short dashed), radiative heating (long dashed) and vertical heat flux convergence (dot dash) in K d^{-1}. Vertical axis: pressure (hPa). (b) Total heating rate due to these four processes (dashed) and mean vertical motion (solid) in units of 0.01 Pa s^{-1}.

has a peak at the same level. The reason may be that tha air near the 0°C level is cooled by mesoscale snow melting, and this cooling has the effect of enhancing subsidence warming because of the greater vertical temperature gradient.

Net mesoscale heating predominates in the upper troposphere around 300–400 hPa (cf. stratiform region's heating profile of Houze 1982). This occurs partially because of vapor deposition onto snow, which falls out of the layer before evaporating, and partially because of deposition onto ice, which forms an expanding cirrus shield so that in both cases deposition outweighs sublimation in the layer.

Radiative cooling of about 2 K d^{-1} through most of the troposphere is mostly due to the clear-air longwave cooling with a small shortwave heating added to it. The clouds only affect the time and spatial average in the high troposphere around 150–200 hPa where long-lived and widespread cirrus exists and is warmed by radiative effects described earlier.

Surface layer vertical heat flux convergence occurs mostly in the cooled downdraft outflow region as it overlies a warmer sea surface and helps to restore the air-sea thermal equilibrium.

Figure 15b shows the total heating and mean vertical motion in the simulation. Heating is concentrated in the layers of net mesoscale and radiative heating in the upper troposphere. The cancellation between convective heating and mesoscale and radiative cooling in the lower troposphere is fairly close leading to a net heating of less than 1 K d^{-1}, compared to 5 K d^{-1} in the upper troposphere. The mean ascent maximum is also located in the upper troposphere showing the atmosphere's response to the heating profile. There is, however, net ascent in the whole troposphere, but this only averages around 1 cm s^{-1}. These figures will be an interesting point of comparison with the results of a no ice simulation described in subsection 8b.

The moistening profile (not shown) is dominated by a net drying of about 10 g kg^{-1} per day in the lowest 2 km due to the convective parameterized subsidence and downdraft transports. There is weak net drying up to 500 hPa as convective-related subsidence cancels mesoscale evaporation but mesoscale deposition adds to net drying above 400 hPa.

The presence of net heating leads to large-scale mean ascent, and cooling and moistening due to vertical advection offsets the heating and drying tendencies described in this subsection.

e. Comparison with WMONEX observations

The simulated system was typical of WMONEX convection, and the model reproduced the overall features well. In particular, the development's time scale and positioning, the propagation and the cloud structure consisting of convective, and mesoscale precipitating regions and a thick cirrus shield were all simu-

lated. The weak convection persisting near the coast also agrees with the observations of Churchill and Houze (1984a).

This study supports the mechanism suggested by Houze et al. (1981) that land-breeze convergence initiates convection. However, once the system has developed, it is the convective downdrafts that provide the localized convergence and the land breeze has no role in the mature and decay stages. The temperature deficit in these downdrafts of around 3°C is in good agreement with surface ship observations during WMONEX.

Quantitatively, estimates from WMONEX observations have a reasonable agreement with the model. Johnson and Young (1983) derive the heating profile in the mature and decaying stages of several WMONEX clusters averaged over the ship triangle (350 km a side). Their results show typical apparent (cumulus plus mesoscale) heat sources around 10–20 K d^{-1} and concentrated in the upper troposphere at 1400 LST, which compares with 18 hours model time. The model still has weak convection at this stage so there is some lower tropospheric heating, but the general mesoscale evaporation cancels its effect. The upper tropospheric cloud is less active than during the mature stage when 20 K d^{-1} was reached but still produces around 5 K d^{-1} heating on a 500 km scale in the model.

Johnson and Young's study shows a mean vertical motion of 0.1 to 0.15 m s^{-1} in the mesoscale updraft averaged over the ship array's area. Churchill and Houze (1984b) also estimate the mesoscale ascent in the stratiform region (their cluster B on 10 December 1978). Their value, based on the ice budget, is between 0.1 and 0.2 m s^{-1}. The simulation's mesoscale ascent remains strong until nearly 18 hours and has a maximum amplitude at around 350 hPa, the magnitude is about half of that estimated by Johnson and Young (1983) but applies to a larger scale. Earlier, at about 12 hours (0800 LST), the maximum ascent is at 450 hPa and has a greater amplitude also in agreement with observations. The upward shift and decrease in the vertical motion maximum at later stages results from the decay of the convective contribution as described by Houze (1982) and the mesoscale cloud mostly determines the large-scale motion at this stage.

Churchill and Houze's (1984a) microphysical observations support the modeling inference that conditions supersaturated with respect to ice, but subsaturated with respect to water, may exist over a wide area in the stratiform cloud. This also places limits on vertical motion magnitudes.

Mesoscale descent is not evident in the domain averaged vertical motion in the decay stage due to the continued presence of low convective updrafts. However, it exists and occurs in a well-defined region throughout the mature and decay stage (seen in Figs. 11a and 13). Observations (Churchill and Houze 1984a; Johnson and Kriete 1982) suggest that warming and drying occur in association with the subsidence in the post-convective lower troposphere. This is a common finding in tropical systems, but there is little evidence of warming in the model even though there is subsidence.

The change in the moist static energy profile after the modeled storm passage implies that a subsidence of several kilometers occurs, but the humidity of this air remains high because, as seen from the initial sounding (Fig. 8), the environmental profile is very humid and nearly moist-adiabatic. To force warm and dry subsidence in this environment a dynamical process may be necessary such as that suggested by Miller and Betts (1977) where midlevel environmental air descends over a cold spreading (and therefore subsiding) density current. The lack of a third dimension may restrict this process. Horizontal pressure gradients generated by the convective region may also be responsible for driving a midlevel subsident rear inflow, as seen in two-dimensional nonhydrostatic numerical squall line modeling studies (e.g., Dudhia et al. 1987; Chen and Cotton 1988), and this fact could partially explain the lack of warm subsidence in the present hydrostatic model.

Johnson and Kriete (1982) noted that before midday the air above 100 hPa typically cools by 6°–10°C. However, the model produced no such cooling suggesting either that its cause is not allowed for in the model parameterizations of ice phase physics and radiation or that there is insufficient vertical resolution. The tropopause is only crudely represented by the model's 53 hPa resolution and so critical vertical temperature gradient changes may be missed. Johnson and Kriete suggest that the cooling appears to occur above, rather than in, the main cloud deck, possibly in a thin stratospheric ice-crystal layer or in upward-forced clear air.

Rainfall in the simulation is generally about half that observed at the ship *Akademik Korolev* which is positioned 150 km off the coast. This may also be a result of the three-dimensionality of the real system. The two-dimensional model assumes that no gradients of variables occur parallel to the coast, whereas in reality they exist because the convective line is of finite extent in this direction. Three-dimensionality is probably particularly important when the post-convective cold pool has been established at the surface. The surface monsoon flow has a strong wind component parallel to the coast and perpendicular to the domain. The advection of unmodified surface boundary layer air into the domain's plane by this wind component tends to restore the post-convective surface layer more quickly than the sea surface fluxes in the model so that new convection may occur, whereas in the model the cold pool would take many hours to be restored to a conditionally unstable layer by the surface heat and moisture fluxes.

Radar observations (Fig. 7) show that the northeastward (i.e., along-coast) extent of the convective region may be limited by the general monsoon flow, and a line of clouds forms upstream of the convective area in response to the convergence. The different orientations of the coastline and monsoon flow convergence make this a difficult system to represent correctly in two dimensions, but the primary purpose of this work was to demonstrate physical mechanisms of mesoscale cloud development. This idealized system removes many of the complications associated with a third dimension and makes understanding the processes easier, but removal of this dimension may have caused overall rainfall to be underestimated.

Several studies have also shown the importance of sustained larger scale vertical motion, not included in this model, that exists particularly in the equatorial region (e.g., Soong and Tao 1980; Dudhia and Moncrieff 1987). Frank and Cohen (1987) impose this effect in their two-dimensional study of tropical convection and Cohen (1989) finds that including it can double the rainfall compared to excluding it even with a mean applied ascent of only 1 cm s^{-1}. A similar sensitivity study with the current model confirmed this potential for larger scale convergence to enhance the rainfall. It was also found that the convective heating strengthened to compensate for the adiabatic cooling resulting from ascent, and deepened because of the reduced stability, with the result that convective heating became much stronger relative to mesoscale latent heating.

8. Sensitivity studies

Several sensitivity studies are required to show how the system's behavior depends upon various physical processes that are parameterized in the model. The primary interest in this study is in the mesoscale resolved clouds, but since the cumulus parameterization has an important part in producing these it is useful to test some of the scheme's parameters.

a. Cumulus parameterization tests

As demonstrated by Frank and Cohen (1985), the lateral detrainment rate assigned to updrafts determines the distribution and magnitude of cumulus heating. Low values of lateral detrainment produce a stronger overall mass flux, especially in the upper troposphere. This is because the detrainment to entrainment ratio, α, determines the shape of the mass flux profile. Since lateral entrainment increases the mass flux with height, greater compensating subsidence occurs at greater heights leading to more heating higher up. However, if lateral detrainment balances lateral entrainment, the updraft mass flux is constant with height and weaker overall. The value of α used in the control simulation is 0.5. A sensitivity study was carried out with α equal to 1, i.e., entrainment and detrainment balance.

The test demonstrated the importance of the mass flux profile of the updrafts in determining the rainfall total. A lower lateral detrainment rate to entrainment rate ratio produces weaker but higher clouds primarily because of the reduction in magnitude of the upper tropospheric mass flux and consequent reduction in subsidence stabilization.

Cohen and Frank (1987) ran a similar sensitivity study, comparing a value of α of 1.25 with one of zero. They find that, although the no detrainment convection is initially stronger, there is less tendency to form mesoscale clouds so the system is shorter lived. This contrasts with the present case, where lower detrainment was more favorable. However, the situation here is different from Cohen and Frank's because convergence is sustained initially by the persistent land breeze, while in their study there is no such continuous localized forcing. The formation of a mesoscale precipitation region with its associated cooling appeared essential in providing the convergence that would lead to a long-lived convective system.

The magnitude of the entrainment rate, ϵ, also affects the mass flux profile, and so changes in its value have a similar general effect to changes in α. In particular, a reduction in entrainment rate produces higher convective clouds but with a weaker upper tropospheric heating.

Another related parameter, β, specifies the ratio of the new updraft mass flux to the mean convergence for a one-dimensional cloud calculation. The value chosen for the simulations is $\beta = 2$. Frank and Cohen use $\beta = 1.25$ with a 20 km grid size. They suggest the β should decrease towards 1 with decreasing grid size but this assumes that all of the updraft mass flux comes from the subcloud layer (lowest 50 hPa) while in some studies (e.g., the numerical modeling study of Dudhia and Moncrieff 1987), there is evidence that net convergence into the updrafts exists throughout the lowest 100 hPa. Setting β greater than 1 indirectly allows for a deeper updraft inflow layer than 50 hPa. There is sensitivity to the value of β, since $\beta = 1$ halves the updraft mass flux for a given convergence compared to the control simulation and produces much weaker convection. Taking $\beta = 4$ overestimates the heating and growth rate and eventually leads to instability in the hydrostatic model. Brown (1979) also finds sensitivity to an equivalent parameter in his updraft-only cumulus parameterization. As Brown points out, setting $\beta > 1$ implies that compensating subsidence occurs at cloud base (500 m) but also allows the convection to grow by creating a warm core at low levels, which in turn induces mesoscale ascent and convergence. There is an important feedback here that needs to be represented realistically and probably requires high resolution cloud modeling or observational studies to determine the parameter properly for various meteorological situations.

A parameter in the cumulus scheme that also affects the development of the mesoscale system is the cloud lifetime, τ. This is the period at a grid point between recalculations of the one-dimensional cloud model and also determines the time delay between an updraft and its corresponding downdraft. Frank and Cohen (1987) specify this according to the updraft rise time of a parcel multiplied by 2, giving lifetimes of around 20 minutes. The parameter, τ, is also a measure of the growth rate of clouds because each time the one-dimensional cloud is recalculated, the mesoscale convergence in the previous ten minutes plus downdraft convergence is used to determine the new mass flux, so that, because of cloud heating, successive calculations at a grid point tend to produce larger clouds until the supply of buoyant low-level inflow is cut off by the downdrafts. To understand the effect of changing this parameter, it is necessary to describe the propagation mechanism of the modeled system.

In all simulations new clouds are first formed by weak convergence (2×10^{-5} s^{-1}) several tens of kilometers ahead of the surface cold air region. The convergence results from deep long gravity waves generated within the active convection region but propagating ahead at 20–30 m s^{-1} and produces small clouds, 2–5 km in height, with low mass fluxes and high entrainment rates. It is these clouds that eventually grow and are absorbed into the propagating convective region. Thus the propagation results more from discrete regeneration ahead of the cold air than forcing by a convective downdraft gust. Surface observations of WMONEX systems may support this conclusion because the strength of surface forward flow associated with the cold downdraft outflow was not greater than the system propagation speed; i.e., the cold air was not overtaking the gust front as would be necessary for a density current forcing, even allowing for surface friction. The production mechanism for the gravity waves here may be related to the cumulus parameterization scheme since the heating rate for given grid column changes suddenly at 40 minute intervals, and the gravity waves could be a means of atmospheric adjustment to the new heating rate. However, in nature, it is possible that there may be a similar response to the rapid growth of new cumulonimbus towers. Gravity waves, as in the theoretical model of Raymond (1975), have often been considered responsible for the discrete propagation observed in squall lines (e.g., see Houze and Betts 1981).

Although clouds are not initiated by the downdraft-produced surface temperature gradient in the model, they are significantly enhanced by the mesoscale convergence maximum that occurs there (2×10^{-4} s^{-1}), so the gust front still has an important role in organizing convection into a small region. However, when a 20 minute lifetime is used, instead of the 40 minutes in the control run, clouds can grow to produce strong downdrafts and updraft heating even before the primary gust front reaches them. This tends to shift the active convection region forward, and hence new clouds form further ahead of the gust front and the effective propagation speed increases from 6–7 m s^{-1} to 9–10 m s^{-1}. This increase in speed makes the mesoscale system more squall-line like in the sense that the mesoscale rainfall now is entirely behind the convective rainfall instead of ahead and behind. The difference is cause by the fact that the system now moves at a speed comparable with the upper winds rather than slower, so that the mesoscale anvil cannot be advected ahead of the convective region. Since the rapid growth of clouds was considered unrealistic in this case, where the initializing convergence is very weak, a 40 minute lifetime was set for all simulation.

The above tests have demonstrated some of the uncertainties associated with cumulus parameterization at this scale, which is still a central problem in mesoscale hydrostatic modeling. However, an advantage of using the Frank and Cohen scheme is that the physical meaning of each of the parameters is fairly apparent and would be easy to interpret against observational or cloud-scale modeling data. Alternatively, it is easier to intuitively assign values to these parameters based on the current understanding of cumulus dynamics. The scheme also maintains realistic thermodynamical properties in the updraft and downdraft outflows and can be used to predict some microphysical properties of the detrained cloud, both crucial requirements for this study of mesoscale cloud development.

b. No ice simulation

A simulation identical to the control was run except that the freezing point was set to 100 K. This has the effect of turning off all ice phase processes and the additional latent heat associated with the ice phase in both the resolved-scale moisture and cumulus parameterization. Only cloud and rain exist and are parameterized as described before.

The overall rainfall in this simulation was only slightly less (95%) than in the ice simulation primarily differing in the decay stage. The overall precipitation content in the domain was from 30%–40% of the control's, mostly because of the reduced fall speed of snow in the control which allows it to accumulate more. The cloud contents in both simulations were similar, but the cirrus cloud extended further than the all-water cloud in the upper troposphere. The mesoscale rain area and rainfall fraction were not significantly different from the control, accounting for 35% of the total rain.

The propagation of both systems was almost identical at about 6–7 m s^{-1}. It is probably this fact that accounts for the small difference in spatial scale of the two rain areas. In faster moving cases such as squall lines, the rearward extension of the mesoscale upper

tropospheric cloud is more strongly determined by the particle fall speeds and mesoscale motion, and this would differentiate more between ice and no ice.

Figures 16a and 16b show that despite the superficial similarities described above, there are some basic differences in the mean properties of the ice and no ice simulations. In the no ice simulation average heating occurs almost exclusively in the high convective updraft regions while resolved-scale net condensation does not occur at any level. This contrasts with the ice simulation where upper tropospheric mesoscale deposition is the most important process in the total heating profile at that level (Fig. 15b) and convective cloud tops tend to be lower possibly because of warming in the stratiform cloud.

Comparison of the mesoscale latent heating curve with that in Fig. 15a shows that the cooling peak around 550 hPa is completely lacking in the no ice case consistent with the fact that it results from melting and with the reduced upper tropospheric stratiform precipitation production. The lower tropospheric mesoscale cooling is similar in both cases because about the same amount of rain falls through this layer and evaporates in each run. The total heating profile in Fig. 16b of the no ice simulation has a maximum in the midtroposphere where rain production is strongest. In the lower troposphere there is a slight net cooling of less than 1 K d^{-1}. Figure 11b shows how the vertical motion in the no ice simulation has a maximum at a significantly lower level than the control shown in Fig. 11a, and the 18-hour mean vertical motion profile in Fig. 16b reflects this fact. Also, the net heating profile shows the no ice case to have a lower level maximum than the ice case.

Radiative heating at the base of high clouds is apparent in both simulations and is responsible for the high troposphere's mesoscale ascent above 250 hPa.

These results confirm that ice has an important effect on the overall heating profile of these tropical systems, shifting the maximum up into the upper troposphere. This is caused by resolved-scale latent heating through the processes of mesoscale deposition onto snow and melting of snow in the midtroposphere where the maximum would be in the absence of ice phase processes. Without ice, much of the condensate released by updrafts in the upper troposphere evaporates rather than forming precipitation, and this has a marked effect on the net heating at those levels.

Two further tests were run, first with the saturated vapor pressure over ice set equal to that over water and then vice versa. The first test produced a net heating profile very similar to that of the no ice case in Fig. 16b with a net heating maximum at 500 hPa. This simple change has thus removed much of the effect of ice by removing the possibility of supersaturation. The convective updrafts would be quite insensitive to the value of ice saturation, so the test showed the importance of processes outside the updrafts to the heating profile. In particular, the difference in saturated vapor pressures in the control results in a transition to ice saturation in a supersaturated mesoscale updraft and provides most of the upper troposphere's extra heating

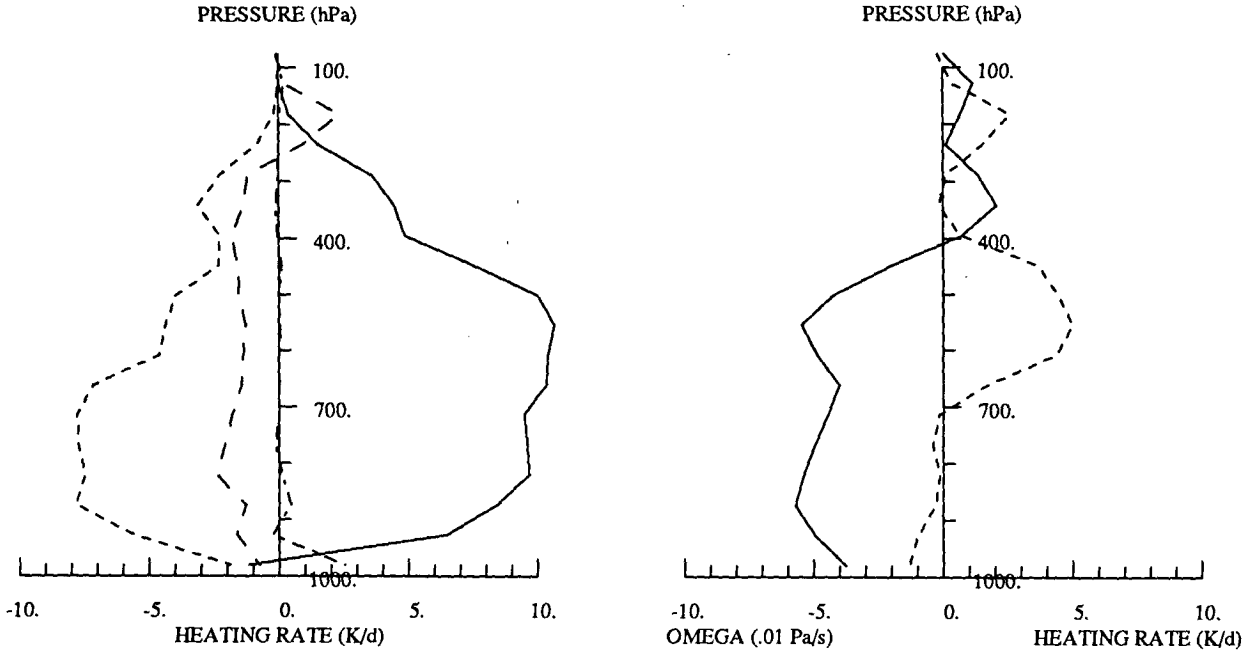

FIG. 16. (a) Heating profiles as in Fig. 15a, and (b) total and mean vertical motion as in Fig. 15b but for no ice simulation.

when ice is present. In the second test, with water saturation reduced to the ice saturated vapor pressure, there was more upper tropospheric ascent and mesoscale latent heating than in the first test. This is as expected since more latent energy is available, but mesoscale latent heating was only half of the control's and the overall heating maximum was still at 500 hPa, again probably because of the lack of supersaturated conditions.

Supersaturation in the mesoscale cloud is apparently efficient in providing net latent heating since precipitation produced must fall out of the layer before any evaporation can occur. Without supersaturation, the snow more readily sublimates, and consistently mesoscale surface rainfall drops by about 30% compared to the control, while convective rainfall remains almost the same.

c. *No radiation simulation*

A simulation was run with the radiative heating and cooling in the atmosphere removed but still acting on the land surface heat budget to provide a land breeze.

The effect of removing radiation from the simulation was to severely restrict convective development. In the first 6–8 hours of the simulation the behavior was similar to that with radiation as is shown by the domain total precipitation content (Fig. 17) compared to the control (Fig. 12). The major difference occurred from 8–12 hours when the control simulation produced a rapidly growing mesoscale system as indicated by Fig. 12. The no radiation simulation failed to grow to the same extent and shallower weaker clouds developed.

The primary effect of radiation at this stage is one of cooling the clear-air region by 2–3 K d^{-1}, thus counteracting the warming resulting from convection. This tends to destabilize the sounding to convection because, although radiative cooling extends to the surface, the sensible heat flux from the surface is slightly stronger when radiative cooling is active, and besides, the updraft temperature is determined partly by its inflow's water vapor content, which is unchanged by radiation. Therefore, the boundary layer's θ_e supplying the updrafts reduces more slowly than the midtropospheric θ_{es} allowing stronger convection.

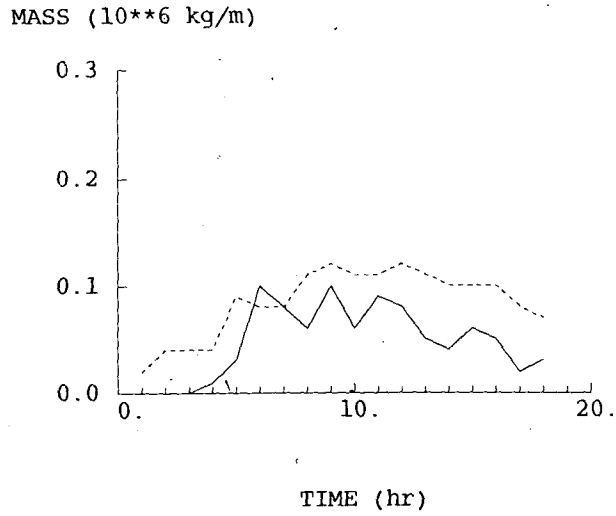

FIG. 17. Domain total precipitation and cloud mass as a function of time as in Fig. 12 in "no radiation" simulation.

From 8 hours onwards the no radiation case went through a gradual decay as the general warming reached typically 1°–2°C throughout the troposphere while in the control run warming was confined mostly to the upper troposphere and was of a lesser magnitude. Figures 18a and 18b show respectively the control and no radiation temperature perturbations from the initial values in the domain at 12 hours.

The results indicate that the convective activity is controlled to a large extent by the general cooling rate of the troposphere from radiative processes. A balance results whereby convective warming and radiative cooling are closely related; stronger radiative cooling permits stronger convection. Cloud modeling studies such as those of Soong and Tao (1980) and Dudhia and Moncrieff (1987) show that the tropospheric cooling rate, which in their cases is due to imposed larger scale convergence in the lower troposphere, can modulate convective activity and the latter study and a hydrostatic model study by Cohen (1989) showed that the cooling alone (without moisture convergence) accounted for about half the enhancement. In the present study it is longwave radiation rather than forced vertical advection that provides the cooling, which is typically about equal to that that would result from forced ascent of 0.5 cm s^{-1}. Chen and Cotton (1988) also find a similar tendency to reduce convective strength when radiative effects are excluded in a 4-h simulation.

As the sun rises shortwave warming reduces tropospheric radiative cooling to less than 1 K d^{-1} so clear-air radiative forcing is significantly reduced during the daytime. The cirrus shield covering the region may reduce this diurnal effect, as it has a strong effect on the shortwave flux below it and only a slight effect on the longwave radiative balance. However, despite such effects the decay of the system was primarily a result of its moving into a less favorable boundary layer as stated earlier.

The no radiation simulation produced a cirrus shield of much smaller extent than the control. This was probably due to the reduced convective activity but may also be the result of lacking the net radiative heating that would maintain it against sublimation by forcing mesoscale ascent.

The propagation speed was reduced to about 5 m s^{-1} (compared to 6–7 m s^{-1}) and the net rainfall, in-

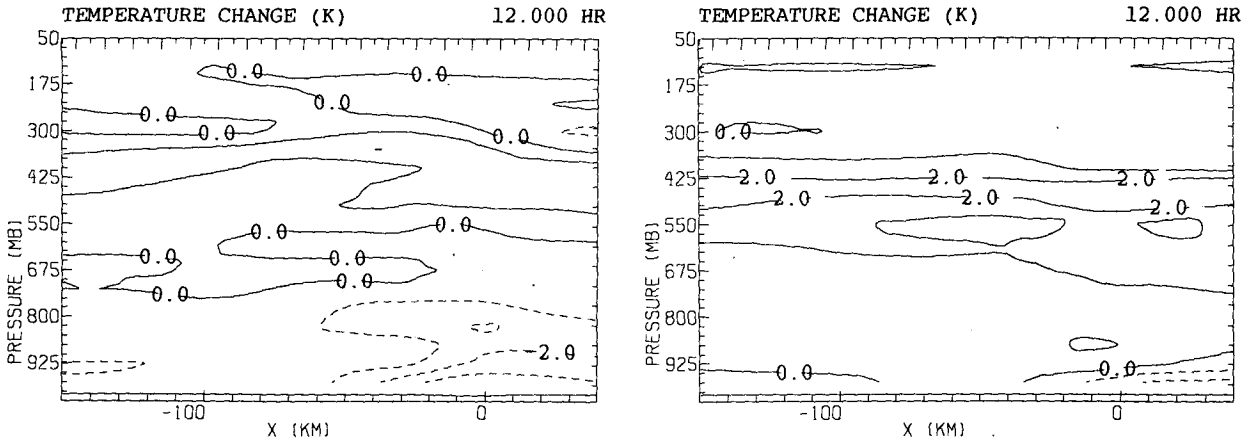

FIG. 18. (a) Temperature perturbation from initial state (deg K) in "control" simulation, and (b) in "no radiation" simulation for the convective area at 12 h. Contour interval 1.0 K.

cluding convective and mesoscale rain, was 36% of the control by 18 hours.

Another simulation was carried out to test the possibility that the importance of radiation is partly due to the cloud/clear-air cooling rate differences as suggested by Gray and Jacobsen (1977) and supported by Cohen and Frank's (1987) simplified radiative test. In this simulation cloud effects were removed by setting the liquid water path to zero irrespective of cloud or precipitation content. The simulation developed a strong convective system and was overall very similar to the control in most respects. The only major difference was that the cirrus extent was reduced by 100 km. This confirms the importance of cloud-radiative interaction in the high troposphere. As shown in section 4, the high moisture content of the tropical lower troposphere reduces cloud base heating significantly below about 400 hPa but in drier mid-latitudes radiation/cloud interactions may additionally be important at lower levels.

The results of this section differ to some extent from the tentative findings of Cohen and Frank (1987). Their results showed that there was an increase in convective strength when they included tropospheric clear-air cooling, cloud base heating and cloud top cooling but that mean cooling had less effect on their simulation than the cloud effects. This contrasts with the finding here that clear-air cooling is vital to the maintenance of active convection. The difference can be explained by the fact that Cohen and Frank have an imposed large-scale lower tropospheric convergence leading to ascent rates of about 1 cm s^{-1}. Their conditional instability is maintained by adiabatic cooling associated with this and has less need of the additional cooling supplied by radiation, whereas in the present study there is no large-scale ascent and radiative cooling proved vital to the system. Cloud base heating in Cohen and Frank's simulation (based on Webster and Stephens 1980) was also several times larger than is produced by the radiative scheme here and so had a proportionately greater effect.

9. Discussion and conclusion

a. Comparison with other studies

The simulated convective system has features comparable with observed tropical systems, many of which include mesoscale downdrafts and updrafts.

In the simulation, it is clear that melting and evaporation of mesoscale rainfall can cause cooling rates around 50 K d^{-1} and drive a mesoscale downdraft of up to 30 cm s^{-1}. Although dynamical forcings such as the spreading cold air pool below and subsident response to nearby convective towers also could contribute, the location of the subsidence favors melting and evaporation as the driving mechanism, as do the thermodynamic properties of the subsiding air. Brown (1979) and Cohen and Frank (1987) have also concluded that moist processes are responsible for the mesoscale downdrafts from their modeling studies. The magnitude of descent in this WMONEX model is consistent with that suggested by Zipser (1977). The suggestion of Leary and Houze (1979) that melting and evaporation are equally important contributors to subcloud cooling also applies to the WMONEX simulation's stratiform region.

Mesoscale ascent magnitudes in the model of up to 50 cm s^{-1} also agree with that generally diagnosed in the upper troposphere associated with convection in midlatitudes (e.g., Ogura and Liou 1980; Smull and Houze 1987) and in the tropics (e.g., Houze and Rappaport 1984; Churchill and Houze 1984b; Chong et al. 1987).

The ascending mesoscale cloud in the upper troposphere can be driven by several destabilizing mechanisms highlighted in this and other studies. Ice-phase and radiative heating have been shown to be potentially important in respectively the stratiform and cirrus clouds in this study, but other models provide different mechanisms. Brown (1979), through detraining heavily water-loaded updraft air, and Cohen and Frank (1987) with high lateral detrainment from the updrafts produce mesoscale thermodynamic profiles that are forced towards unstable stratification by the accumulation of air with a higher θ_e near the base of the stratiform cloud. This drives mesoscale motion to enable the potentially warm air to rise to an equilibrium level with respect to the larger scale environment.

The inclusion of more detailed ice phase and radiative processes in this study make the necessity of detraining high θ_e air below its level of thermal equilibrium less important because it is possible for the mesoscale cloud itself to warm up. So, although liquid/ice-loading and lateral detrainment have a role in the model's mesoscale ascent, they are not as important as in these previous studies. The no ice simulation, in particular, demonstrated the relative importance of mesoscale latent heating in driving upper tropospheric ascent.

The heating profile over the lifetime of the system supports the finding of Houze (1982) that the upper tropospheric net heating comes from the mesoscale anvil while lower tropospheric mesoscale evaporation strongly opposes the convective heating leaving a maximum heating influence in the upper troposphere.

The proportions of stratiform and convective rainfall in the model (35% and 65%) are in the range of those deduced by Houze and Rappaport (1984; 42% stratiform) for a slow GATE line, Churchill and Houze (1984a; 46%) for WMONEX case, Chalon et al. (1988; 20%) for a West African case and many other observational studies. Much of the stratiform precipitation is generated within the mesoscale updraft, but detrainment of air containing graupel or snow from the convective region is essential to initiate such rainfall as suggested by Rutledge and Houze (1987). The magnitudes of precipitating and cloud ice contents were very similar to those in their kinematic study.

Propagation in the model by long gravity waves generated within the convective region and moving ahead is similar to that found by Crook and Moncrieff (1988) in their model. Houze and Betts (1981) also suggested that such waves may offer an explanation for the discrete propagation of some GATE squall lines.

b. *Conclusions*

The simulation has reproduced, realistically, most of the convective features of the system observed over the South China Sea during WMONEX. In this study emphasis has been given to the physical processes that drive motion on the model's resolved scale in an effort to examine the interaction between the heating they produce and the large-scale upward and downward motion. The main results can be summarized as follows:

1) Land-breeze related convergence by differential cooling of the ocean and land surface produced the initial convection near the coast.

2) New cells develop upstream of the existing convective area relative to the low-level wind direction.

3) Propagation appears to be by discrete jumps associated with long gravity waves moving ahead of the convective region but generated within it. There is also a cold surface pool that enhances convergence on the upwind side of the major updrafts. The overall propagation speed of 6–7 m s^{-1} agrees with observations but depends strongly on the model's cloud lifetime parameter, which influences the parameterized convective growth rate.

4) Ice phase processes contribute most strongly in a layer between 0° and −20°C where mesoscale ascent is forced by the slow release of latent heat by deposition onto snow. Mesoscale ascent is strongest during the later part of the mature phase. Mesoscale subsidence appears to be driven both by melting and evaporative cooling and is thus concentrated to the rear of the convective area. However warm mesoscale subsidence is lacking in the model, probably because of the model's limitation to two dimensions.

5) Net radiative heating becomes important in the late morning and is particularly strong in regions of high cloud base, namely the extending cirrus shield, where longwave cloud base warming is maximized, and cooling at cloud top is offset by solar irradiation.

6) Clear-air longwave cooling proved vital to the system's intensification because of the marginal conditional instability of the initial sounding. It appears that even on time scales of 6 hours, this tropospheric cooling can make the difference between strong and weak convection.

7) The system finally decays on meeting less favorable boundary layer air around 400 km offshore associated with lower sea surface temperatures. The observed decay was quicker than that modeled, possibly because of the air in the model being initialized horizontally uniformly and not taking into account larger scale advection.

8) The final rain totals from the model show 35% to have been mesoscale in character and 65% convective, but somewhat underestimated compared to observations possibly because of the lack of the third dimension or larger scale convergence.

9) The overall heating and mesoscale ascent of the model system were concentrated in the upper tropo-

sphere and distinctly different from a no ice simulation where both maxima were shifted downward into the midtroposphere and where the differences due to the lack of supersaturation and melting were conspicuous in the mesoscale latent heating profile.

The goal of this study was to develop and employ a mesoscale model capable of representing these tropical convective clusters in sufficient detail to answer several questions regarding their development and maintenance. In this work, the mechanisms leading to mesoscale motion are clarified by use of sophisticated parameterization schemes that can show the potential of various processes to produce mesoscale heating under realistic atmospheric conditions and fully interacting with each other.

The model will be further developed and applied to other convective situations such as the recently obtained Equatorial Mesoscale Experiment (EMEX) data where more in-cloud measurements of microphysical and radiative properties should be useful for comparison with the parameterization scheme and may lead to improvements.

Acknowledgments. This study was carried out while the author was a post-doctoral fellow of the Low Frequency Dynamics Group and the Earth's Systems Science Center at The Pennsylvania State University. The author would like to thank Professors P. J. Webster and E. Barron for their support. The research was also supported by the Office of Naval Research under Grant N0014-86-K-0688 for Fleet Scale Marine Meteorology and by the National Science Foundation through Grant ATM-8617118 for the Equatorial Mesoscale Experiment (EMEX).

The computing was mostly carried out on the Pittsburgh Supercomputer Center's CRAY X-MP funded by the National Science Foundation on Grants PSCA 218 and ATM-0/870008P.

I am very grateful to Peter Webster, Graeme Stephens, William Frank and Charles Cohen for their help in various parts of this work and to the reviewers whose comments improved the paper. Thanks also to Spiros Geotis and Stanley Goldenberg for providing radar and satellite images, and to Hong Yan for the model graphics program. The World Data Center-A, Asheville, North Carolina, supplied winter MONEX ship data.

APPENDIX A

The Mesoscale Model Equations

The Penn State model is based on the primitive equations with a hydrostatic approximation applied to the vertical momentum equation. In σ-coordinates and two dimensions the basic predictive equations are

a. Prognostic and diagnostic equations

- Momentum:

$$\frac{\partial}{\partial t}p^*u = -\frac{\partial}{\partial x}p^*uu - \frac{\partial}{\partial \sigma}p^*\dot{\sigma}u - \frac{\sigma R_d T p^*}{p}\frac{\partial p^*}{\partial x} - p^*\frac{\partial \phi}{\partial x} + fp^*(v - v_g) + p^*(F_u + D_u + P_u + C_u) \quad \text{(A1)}$$

$$\frac{\partial}{\partial t}p^*v = -\frac{\partial}{\partial x}p^*uv - \frac{\partial}{\partial \sigma}p^*\dot{\sigma}v - fp^*(u - u_g) + p^*(F_v + D_v + P_v + C_v). \quad \text{(A2)}$$

- Mass Continuity:

$$\frac{\partial p^*}{\partial t} = -\frac{\partial}{\partial x}p^*u - \frac{\partial}{\partial \sigma}p^*\dot{\sigma} = -\int_0^1 \frac{\partial}{\partial x}p^*ud\sigma, \quad \text{(A3)}$$

where $\dot{\sigma} = 0$ at $\sigma = 0, 1$.

- Temperature:

$$\frac{\partial}{\partial t}p^*T = -\frac{\partial}{\partial x}p^*uT - \frac{\partial}{\partial \sigma}p^*\dot{\sigma}T + \frac{p^*R_dT\omega}{c_pp} + \frac{p^*Q}{c_p} + p^*(F_T + D_T + P_T + C_T + R_T). \quad \text{(A4)}$$

- Water vapor:

$$\frac{\partial}{\partial t}p^*q_v = -\frac{\partial}{\partial x}p^*uq_v - \frac{\partial}{\partial \sigma}p^*\dot{\sigma}q_v + p^*(-\text{PRE} - \text{PRD} - \text{PRI} - \text{PCON} + F_{qv} + D_{qv} + P_{qv} + C_{qv}). \quad \text{(A5)}$$

- Precipitation:

$$\frac{\partial}{\partial t}p^*q_r = -\frac{\partial}{\partial x}p^*uq_r - \frac{\partial}{\partial \sigma}p^*\dot{\sigma}q_r - \frac{\partial}{\partial \sigma}V_f\rho gq_r + p^*(\text{PRE} + \text{PRC} + \text{PRA} + F_{qr} + D_{qr} + C_{qr}). \quad \text{(A6)}$$

- Cloud:

$$\frac{\partial}{\partial t}p^*q_c = -\frac{\partial}{\partial x}p^*uq_c - \frac{\partial}{\partial \sigma}p^*\dot{\sigma}q_c + p^*(\text{PRD} + \text{PRI} - \text{PRC} - \text{PRA} + \text{PCON} + F_{qc} + D_{qc} + P_{qc} + C_{qc}). \quad \text{(A7)}$$

The terms F, D, P, C, R are respectively horizontal eddy diffusion, horizontal fourth order smoothing, vertical eddy flux convergence (including surface flux), cumulus transport term, and radiative heating. The moist processes (PCON, PRA, PRC, PRD, PRE, PRI) are defined in appendix B. Here Q is the latent heating rate due to PCON, PRD, PRE, PRI and melting/freezing, and V_f is the mass-weighted fall speed of rain.

The hydrostatic equation for geopotential height is

$$\frac{\partial \phi}{\partial \ln(\sigma + p_t/p^*)} = -R_d T_v. \tag{A8}$$

The virtual temperature, $T_v = T(1 + 0.608q_v)$.

The vertical sigma-velocity, $\dot{\sigma}$, is diagnosed from the mass continuity relation (A3):

$$\sigma = \frac{p - p_t}{p_s - p_t} \tag{A9}$$

$$p^* = p_s - p_t, \tag{A10}$$

where p_s and p_t are respectively the pressure at the surface and the top of the model, the latter being constant. Omega, the pressure velocity, is obtained from

$$\omega = p^*\dot{\sigma} + \sigma\left(\frac{\partial p^*}{\partial t} + u\frac{\partial p^*}{\partial x}\right). \tag{A11}$$

b. Parameterized processes

The surface sensible heat flux, latent heat flux, and stress are given by

$$H = \rho_s c_p u_*^2(\theta_s - \theta_m)/V_m \tag{A12}$$

$$L = \rho_s L_v \alpha u_*^2(q_{ss} - q_m)/V_m \tag{A13}$$

$$\tau = \left(-\rho_s u_*^2 \frac{u_m}{V_m}, -\rho_s u_*^2 \frac{v_m}{V_m}\right) \tag{A14}$$

$V_m = |\mathbf{v}_m|$ where $\mathbf{v}_m = (u_m, v_m)$ is the wind speed, subscript m denotes the lowest grid point, subscript s denotes surface, and q_{ss} is the saturated water vapor mixing ratio at the surface temperature. Here α is the moisture availability that tends towards 1 for wet surfaces and is taken as 0.86 for the tropical forest.

The friction velocity, u_*, is calculated from

$$u_* = \frac{kV_m}{\ln \dfrac{z_m}{z_0}}, \tag{A15}$$

where z_0 is a roughness length, z_m is the height of the lowest grid point (typically 235 m), and k is von Karman's constant. For this study, in the above equations u_*^2 is enhanced or reduced by the layer's shear and stability through a factor $(1 - \mathrm{Ri})$ where Ri is the Richardson number.

For the ocean z_0 is dependent on u_*, as defined by Zhang and Fritsch (1986). This allows for the effects of waves generated by boundary layer turbulence. For land z_0 is taken to be 6 cm. All the vertical gradients are taken between lowest grid point and the surface, where the temperature equals the surface temperature and the velocity is zero.

The K coefficient for vertical turbulent mixing above the boundary layer is given by Zhang and Fritsch as a modification of the scheme of Anthes and Warner (1978),

$$K_z = \begin{cases} K_0 + \left|\dfrac{\partial \mathbf{v}}{\partial z}\right|(k\Delta z)^2(R_c - \mathrm{Ri})/R_c, & \text{for } \mathrm{Ri} < R_c \\ K_0, & \text{for } \mathrm{Ri} \geq R_c. \end{cases} \tag{A16}$$

Here $R_c = 1$, $K_0 = 1\ \mathrm{m^2\ s^{-1}}$ and Δz is the vertical grid length. A new feature is that in evaluating the Richardson number in resolved-scale cloudy regions (>0.5 g kg^{-1}), the possibility of moist-adiabatic turbulence is allowed for by defining Ri as

$$\mathrm{Ri} = \begin{cases} \dfrac{g}{\theta}\left(\dfrac{\partial \theta}{\partial z} - \Gamma\right)\left(\left|\dfrac{\partial \mathbf{v}}{\partial z}\right|^2\right)^{-1} & \text{for cloudy regions} \\ \dfrac{g}{\theta}\left(\dfrac{\partial \theta}{\partial z}\right)\left(\left|\dfrac{\partial \mathbf{v}}{\partial z}\right|^2\right)^{-1} & \text{for clear regions} \end{cases} \tag{A17}$$

where $\Gamma = (\partial\theta/\partial z)_{\mathrm{wet}}$ is the θ lapse rate following a moist adiabat.

The coefficient for fourth-order diffusion is 96% of that which completely removes two-grid-length waves and is necessary for numerical stability.

Horizontal turbulent diffusion is parameterized by a second order diffusive term:

$$\left(\frac{\partial \phi}{\partial t}\right)_d \equiv D_\phi = \frac{\partial}{\partial x} K_x \frac{\partial \phi}{\partial x} \tag{A18}$$

$$K_x = (c\Delta)^2\left(\delta^2 + \left|\frac{\partial \mathbf{v}}{\partial z}\right|^2\right)^{1/2} \tag{A19}$$

$$\Delta^2 = \Delta x \Delta z.$$

The value of Δz in this equation is reduced in the surface layer to account for smaller eddy sizes but otherwise corresponds to the vertical grid size. Also different from previous formulations of this model, δ^2 is a small constant compared to $|\partial \mathbf{v}/\partial z|^2$ and represents other terms in the three-dimensional deformation, and $c = 0.2$. As with the fourth-order diffusion, this scheme is applied to horizontal gradients on pressure surfaces, not σ-surfaces which slope over sloped terrain. This is achieved by vertical linear interpolation at neighboring grid points from σ-surfaces to the pressure surface corresponding to that of the grid point under consideration.

APPENDIX B

Moisture Scheme

The ice phase parameterization closely follows that of Rutledge and Hobbs (1983) and Lin et al. (1983).

The explicit moisture scheme in the Penn State model is that of Hsie et al. (1984) and is included here for completeness.

a. Cloud processes

The latent heat, L, is defined as L_v or L_s depending on temperature. Here L_v follows Kirchhoff's law and is thus linearly dependent upon temperature, $L_v = L_0 - L_1 T$, while L_s is constant.

Above water saturation, for $T > -40$°C, immediate cloud formation occurs together with freezing below 0°C. The term PCON in the model equations (appendix A) represents the change in water vapor mixing ratio during this adjustment process that occurs within one time step (10 s). Evaporation of cloud at temperatures higher than 0°C is also immediate in conditions subsaturated with respect to water. At temperatures below freezing point, the cloud is assumed to be ice and the sublimation/deposition process, PRD, acts dependent upon the saturation state with respect to ice.

The saturated vapor pressures with respect to water and ice are respectively

$$e_{sw}(T) = 6.1078\left(\frac{T_0}{T}\right)^{5.138} \exp\left[6827\left(\frac{1}{T_0} - \frac{1}{T}\right)\right] \text{ hPa} \quad \text{(B1)}$$

$$e_{si}(T) = 6.107 \exp\left[6150\left(\frac{1}{T_0} - \frac{1}{T}\right)\right] \text{ hPa}, \quad \text{(B2)}$$

where $T_0 = 273.16$ K.

PRI, the initiation of ice crystals, employs Fletcher's (1962) formula for number of ice nuclei per unit mass of air,

$$n_c = 10^{-2} \exp[0.6(T_0 - T)]/\rho \quad \text{kg}^{-1}. \quad \text{(B3)}$$

Initiation includes a parameter $M_0(10^{-12}$ kg), which is assumed to be the initial mass of a new ice crystal:

$$\text{PRI} = \max[(M_0 n_c - q_c)/\Delta t, 0], \quad \text{(B4)}$$

followed by the constraint that

$$\text{PRI} = \min[\text{PRI}, (q_v - q_{si})/\Delta t], \quad \text{(B5)}$$

where Δt is the time step. max[a, b] and min[a, b] refer to the maximum and minimum of the values of the arguments, "a" and "b."

The diameter–mass relation for an ice crystal is taken from Rutledge and Hobbs (1983) who give, for a hexagonal plate

$$D_i = 16.3 M_i^{1/2}. \quad \text{(B6)}$$

The deposition rate is then determined by a method of diffusional balance using the average crystal mass and following Mason (1971) and others,

$$\text{PRD} = \frac{4 D_i (S_i - 1)\rho n_c}{A + B}, \quad \text{(B7)}$$

where $S_i = q_v/q_{si}$:

$$A = \frac{L_s^2 \rho}{K_a R_v T^2}, \quad B = \frac{1}{q_{si}\chi}. \quad \text{(B8)}$$

Here K_a is the thermal conductivity of air and χ is the diffusivity of water vapor in air. The rate of this process is restricted as with PRI to avoid overshooting into ice subsaturation in one time step. This formula also applies in subsaturated conditions where it is negative and represents the sublimation of ice crystals.

Conversion of cloud to precipitation depends on a maximum diameter (500 μm) for ice crystals and a critical liquid content for cloud water. For ice

$$\text{PRC} = \max[(q_c - M_{\max} n_c)/\Delta t, 0]. \quad \text{(B9)}$$

For cloud water

$$\text{PRC} = \max[k_1(q_c - q_{\text{crit}}), 0]. \quad \text{(B10)}$$

b. Precipitation processes

Rain and snow are assumed to have Marshall–Palmer size distributions of the form

$$n(D)dD = N_0 \exp(-\lambda D)dD, \quad \text{(B11)}$$

where D is diameter, λ is the "slope," and N_0 is the intercept. The value of N_{0r} for rain is 8×10^6 m^{-4}. Applying this distribution to snow is a less acurate approximation than for rain, but with N_{0s} set to 2×10^7 m^{-4}, values of particle concentration from 5 to 10 per liter result from typical snow concentrations of 0.1 to 1 g kg^{-1}, which are in reasonable agreement with observation. From this

$$\lambda = \left(\frac{\pi \rho_r N_0}{\rho q_r}\right)^{1/4} \quad \text{(B12)}$$

where ρ_r is the particle density, 100 kg m^{-3} for snow, and 1000 kg m^{-3} for rain.

The fall speed of rain is taken as $V(D) = 842 D^{0.8}$ m s^{-1} and for snow $V(D) = 11.72 D^{0.41}$ from Locatelli and Hobbs (1974). These have a pressure dependence factor $(p_0/p)^{0.4}$. Here p_0 is 1000 hPa. The ventilation factors take the form

$$F = f_1 + f_2 S_c^{1/3} \text{Re}^{1/2}, \quad \text{(B13)}$$

where f_{1r} and f_{2r} take the values 0.78 and 0.32 for rain and f_{1s} and f_{2s} are respectively 0.65 and 0.44 for snow. Here S_c is the Schmidt number, $\mu/\rho\chi$, where μ is the dynamic viscosity of air, and Re is the Reynolds number, $V(D)D\rho/\mu$. The formula for PRE for rain is

$$\mathrm{PRE} = \frac{2\pi N_{0r}(S_w - 1)}{A' + B'} \times \left[\frac{f_{1r}}{\lambda^2} + f_{2r}\left(\frac{a_r\rho}{\mu}\right)^{1/2} S_c^{1/3}\left(\frac{p_0}{p}\right)^{0.2} \frac{\Gamma(c_r)}{\lambda^{c_r}}\right], \quad \text{(B14)}$$

where $c_r = 2.9 = (5 + b_r)/2$, $b_r = 0.8$ is the exponent and $a_r = 842$ is the multiplier in the rain fall-speed formula (see above). Here A' and B' are the same as A and B, but L_s becomes L_v and q_{si} becomes q_{sw}. Here Γ represents the gamma-function. For snow, there is a similar formula for deposition/sublimation with respect to ice saturation, except with 4 replacing 2π.

The accretion of cloud ice by snow and of cloud water by rain are parameterized similarly to each other:

$$\mathrm{PRA} = \frac{1}{4}\rho\pi a' q_c E N_0\left(\frac{p_0}{p}\right)^{0.4} \frac{\Gamma(3 + b')}{\lambda^{3+b'}}, \quad \text{(B15)}$$

where a' and b' are the constants in the fall-speed expression for rain or snow $V = a'D^{b'}$. The efficiency factor, E, is 1 for rain/cloud accretion and 0.1 for snow/ice accretion.

c. Melting and freezing

This is represented by the rate at which particles are advected or fall through the 0°C level.

The rate of melting due to fall is given by

$$\mathrm{PRM} = -\frac{\rho g V_f q_r}{\Delta p}, \quad \text{(B16)}$$

where Δp is the thickness of the grid level and V_f is the fall speed (positive downward). Similarly the advective melting/freezing rate is

$$\mathrm{PRF} = -\frac{\omega(q_r + q_c)}{\Delta p}, \quad \text{(B17)}$$

where ω is the pressure-velocity, melting is negative and freezing is positive, consistent with the other processes where evaporation and sublimation are negative and condensation and deposition are positive.

The latent heating term, Q, in the temperature equation (A4) is given by

$$Q = L(\mathrm{PRE} + \mathrm{PRD} + \mathrm{PRI} + \mathrm{PCON}) + L_m(\mathrm{PRM} + \mathrm{PRF}) \quad \text{(B18)}$$

$$L = \begin{cases} L_v & \text{if } T > 0°\mathrm{C} \\ L_s & \text{if } T < 0°\mathrm{C} \end{cases} \quad \text{(B19)}$$

$$L_m = L_s - L_v. \quad \text{(B20)}$$

The fall speed, V_f, which appears in (B16) and (A6) the predictive equation for q_r is mass-weighted and calculated from

$$V_f = a'\frac{\Gamma(4 + b')}{6}\lambda^{-b'}\left(\frac{p_0}{p}\right)^{0.4}. \quad \text{(B21)}$$

APPENDIX C

Radiative Scheme

Particularly important absorbers of infrared radiation are water vapor, water, ice and carbon dioxide. Visible radiation is absorbed to a lesser extent by water vapor, but clouds act to strongly scatter it enhancing absorption by increasing its path length. The basis of both schemes is to calculate the transfer of radiation at each model level, including longwave emission and shortwave reflection, and the net absorption at each level results in radiative heating. For softwave radiation, only a downward beam is considered, but the solar angle is important. For longwave radiation, both upward and downward fluxes are evaluated and represent hemispheric integrations of diffuse radiation.

a. Longwave radiative scheme

Longwave absorption by water vapor, the primary clear-air absorber, is strongly spectral in character, and the method employed is the commonly used broadband emissivity method (see Stephens 1984). This involves using a precalculated emissivity function, ϵ, which represents the frequency-integrated absorption spectrum of water vapor weighted by a suitable envelope function. Rodgers (1967) gives an upward and downward emissivity as a function of water vapor path, u, with a temperature correction term where u includes a pressure correction factor. The form of the fitted function is

$$\epsilon(u) = \sum_{i=0}^{i=4} (a_i + \bar{T}b_i)x^i, \quad \text{(C1)}$$

where $x = \ln u$ and $\bar{T}$ is a u-weighted $T - 250$ K. For u less than 10 g m^{-2}, the form is

$$\epsilon(u) = \sum_{i=1}^{i=4} (c_i + \bar{T}d_i)y^i, \quad \text{(C2)}$$

where $y = u^{1/2}$. a_i, b_i, c_i and d_i are constants. In the tropics, e-type absorption is an important additional component of the longwave absorption spectrum and is included with a similar fourth-order polynomial in $\ln(ue)$ to (C1) from Stephens and Webster (1979), where e is the partial pressure due to water vapor. Given the emissivity functions, the upward and downward fluxes at any model level are given by

$$F_u = \int_0^1 B(T)\,d\epsilon_u \quad \text{(C3)}$$

$$F_d = \int_0^1 B(T)\,d\epsilon_d \quad \text{(C4)}$$

where in (C3) the integration is taken downwards through the model layers, calculating $d\epsilon$ for each layer and using the temperature T of the layer and the fre-

quency-integrated Planck function, $B = \sigma T^4$, and σ is Stefan's constant. When the surface is encountered, the ground emission F_{bot} is multiplied by $1 - \epsilon$ and added to the integration. In (C4) the integration is taken upwards; downward longwave flux at the model top is assumed to result only from CO_2 emission in the stratosphere. It can be seen from the formulae that if the emissivity reaches 1 during the integration, the atmosphere beyond that makes no contribution to the flux. This is consistent with the idea that an emissivity of 1 corresponds to a "black" layer with respect to longwave radiation.

Following Stephens (1978), the cloud water is assumed to have a constant absorption coefficient which is slightly different for upward and downward radiation. The absorption coefficients are, $\alpha_{cu} = 0.130$ and $\alpha_{cd} = 0.158$ m^2 g^{-1}. To combine these with water vapor absorption, the transmissions are multiplied since clouds are assumed "grey bodies." The net emissivity is then

$$\epsilon_{\text{tot}} = 1 - T_v T_c \tag{C5}$$

$$T_v = 1 - \epsilon_{\text{vapor}} \tag{C6}$$

$$T_c = \exp(-\alpha_c u_c), \tag{C7}$$

where u_c is the cloud water path (liquid mass per unit area).

Ice cloud is assumed to be composed of hexagonal plate-like crystals with the diameter-mass relation given in appendix B. If the assumption is made that the crystals do not reflect longwave radiation and are sufficiently thick to be "black," it is possible to estimate an absorption coefficient as an integrated cross-sectional area. Allowing for the random orientation of these plates and the hemispheric integration factor, 1.66, the absorption coefficient takes a value of $\alpha_i = 0.0735$ m^2 g^{-1} or about half of that of cloud water. Since this value agrees with some observations (Griffith et al. 1980), it was applied in the model.

For rain and snow the size distribution is necessary since the cross section is not proportional to the mass of a particle. The size spectrum changes with precipitation intensity so the absorption coefficient varies with precipitation amount. This is accounted for in the following definition. The effective absorption coefficient is given by

$$\alpha_p = \frac{1.66}{2000}\left(\frac{\pi N_0}{\rho_r{}^3}\right)^{1/4} \text{m}^2\,\text{g}^{-1}, \tag{C8}$$

where ρ_r is the particle density as in (B12). The absorption coefficients are constants with values of 2.34×10^{-3} for snow and 0.330×10^{-3} m^2 g^{-1} for rain. The effective water path length for a layer Δz meters thick is given by

$$u_p = (\rho q_r)^{3/4}\Delta z \times 1000 \text{ g m}^{-2} \tag{C9}$$

so that the transmission is given by

$$T_p = \exp(-\alpha_p u_p). \tag{C10}$$

This transmission function is multiplied with the others in (C5) to give ϵ_{tot}. This is known as an overlap approximation. Rain and snow have less effect on the longwave flux than cloud by 2 to 3 orders of magnitude but still are not insignificant.

Carbon dioxide is less easily treated since it cannot be assumed "grey" because its absorption is concentrated in a band of infrared wavelengths. To include its effect, an overlap method is used as discussed by Stephens (1984). In effect, the spectrum is divided into a carbon dioxide band and a noncarbon dioxide region. The former requires overlapping of the carbon dioxide transmission function while the latter does not. The relative weights of these two regions is slightly temperature dependent, but they add to give the total absorption.

Having obtained the flux profiles, F_u and F_d, the heating rate is defined from

$$R_T = \frac{\partial T}{\partial t} = \frac{1}{\rho c_p}\frac{\partial}{\partial z}(F_d - F_u) = -\frac{g}{c_p}\frac{\partial}{\partial p}(F_d - F_u). \tag{C11}$$

In the model the values of F are defined between the model layers where T and q are defined. This makes the various integrations and derivatives easier to represent numerically.

b. *Shortwave radiative scheme*

The downward component of shortwave flux is evaluated taking into account the effects of solar zenith angle, which reduces the downard component and increases the path length; clouds, which have an albedo and absorption; and clear air, where there is scattering and water vapor absorption. Thus,

$$S_d(z) = \mu S_0 - \int_z^{\text{top}} (dS_{cs} + dS_{ca} + dS_s + dS_a), \tag{C12}$$

where μ is the cosine of the solar zenith angle and S_0 is the solar constant.

As with the longwave scheme, cloud fraction in a grid box is either 0 or 1 because of the assumed stratiform nature of the clouds. The cloud back-scattering or albedo and absorption are bilinearly interpolated from tabulated functions of μ, and $\ln(w/\mu)$ (where w is the vertically integrated liquid water path) derived from Stephens' (1978) theoretical results. The total effect of a cloud or multiple layers of cloud above a height z is found from the above function as a percentage of the downward solar flux absorbed or reflected. Then at a height $z - \Delta z$, a new total percentage

is calculated allowing the effect of the layer Δz to be estimated. However, this percentage is only applied to $\mu S_0 - \Delta S$ (*clear air*), i.e., the clear-air effect above z is removed.

Clear-air water vapor absorption is calculated as a function of water vapor path allowing for solar zenith angle. The absorption function is from Lacis and Hansen (1974). The method is a similar integration-difference scheme to that described for cloud above.

Clear-air scattering is taken to be uniform and proportional to the atmosphere's mass path length, again allowing for the zenith angle, with a constant giving 10% scattering in one atmosphere.

The heating rate is then given by

$$R_T = R_T(\text{longwave}) + \frac{1}{\rho c_p}\frac{\partial}{\partial z} S_{\text{abs}} \qquad \text{(C13)}$$

where S_{abs} is defined from the absorption part of the S_d integral given in (C12) since only cloud and clear-air absorption contribute to solar heating.

The solar and infrared fluxes at the surface, calculated from the atmospheric radiative schemes, are used in the energy budget of the land surface.

REFERENCES

Anthes, R. A., and T. T. Warner, 1978: Development of hydrodynamical models suitable for air pollution and other mesometeorological studies. *Mon. Wea. Rev.*, **106,** 1045–1078.

Brown, H. A., and K. A. Campana, 1978: An economical time-differencing system for numerical weather prediction. *Mon. Wea. Rev.*, **106,** 1125–1136.

Brown, J. M., 1979: Mesoscale unsaturated downdrafts driven by rainfall evaporation: A numerical study. *J. Atmos. Sci.*, **36,** 313–338.

Chalon, J.-P., G. Jaubert, F. Roux and J.-P. Lafore, 1988: The West African squall line observed on 23 June 1981 during COPT 81: Mesoscale structure and transports. *J. Atmos. Sci.*, **45,** 2744–2763.

Chen, S., and W. R. Cotton, 1988: The sensitivity of a simulated extratropical mesoscale convective system to longwave radiation and ice-phase microphysics. *J. Atmos. Sci.*, **45,** 3897–3910.

Chong, M., P. Amayenc, G. Scialom and J. Testud, 1987: A tropical squall line observed during the COPT 81 experiment in West Africa. Part I: Kinematic structure inferred from dual-Doppler radar data. *Mon. Wea. Rev.*, **115,** 670–694.

Churchill, D. D., and R. A. Houze, Jr., 1984a: Development and structure of winter monsoon cloud clusters on 10 December 1978. *J. Atmos. Sci.*, **41,** 933–960.

——, and ——, 1984b: Mesoscale updraft magnitude and cloud-ice content deduced from the ice budget of the stratiform region of a tropical cloud cluster. *J. Atmos. Sci.*, **41,** 1717–1725.

Cohen, C., 1989: Numerical experiments showing the response of parameterized convection to large-scale forcing. *J. Atmos. Sci.*, **46,** 132–149.

——, and W. M. Frank, 1987: Simulation of tropical convective systems. Part II: Simulations of moving cloud lines. *J. Atmos. Sci.*, **44,** 3800–3820.

Crook, N. A., and M. W. Moncrieff, 1988: The effect of large-scale convergence on the generation and maintenance of deep moist convection. *J. Atmos. Sci.*, **45,** 3606–3624.

Dudhia, J., and M. W. Moncrieff, 1987: A numerical simulation of quasi-stationary tropical convective bands. *Quart. J. Roy. Meteor. Soc.*, **113,** 929–967.

——, —— and D. W. K. So, 1987: The two dimensional dynamics and simulation of West African squall lines. *Quart. J. Roy. Meteor. Soc.*, **113,** 121–145.

Fletcher, N. H., 1962: *The Physics of Rainclouds.* Cambridge University Press, 386 pp.

Frank, W. M., and C. Cohen, 1985: Properties of tropical cloud ensembles estimated using a cloud model and an observed updraft population. *J. Atmos. Sci.*, **42,** 1911–1928.

——, and ——, 1987: Simulation of tropical convective systems. Part I: A cumulus parameterization. *J. Atmos. Sci.*, **44,** 3787–3799.

Gamache, J. F., and R. A. Houze, Jr., 1982: Mesoscale air motions associated with a tropical squall line. *Mon. Wea. Rev.*, **110,** 118–135.

Gray, W. M., and R. W. Jacobsen, 1977: Diurnal variation of deep cumulus convection. *Mon. Wea. Rev.*, **105,** 1171–1188.

Griffith, K., S. K. Cox and R. G. Knollenberg, 1980: Infrared properties of tropical cirrus clouds inferred from aircraft measurements. *J. Atmos. Sci.*, **37,** 1077–1087.

Houze, R. A., Jr., 1982: Cloud clusters and large-scale vertical motions in the tropics. *J. Meteor. Soc. Japan,* **60,** 396–410.

——, and A. K. Betts, 1981: Convection in GATE. *Rev. Geophys. Space Phys.*, **19,** 541–576.

——, and E. N. Rappaport, 1984: Air motion and precipitation structure of an early summer squall line over the eastern tropical Atlantic. *J. Atmos. Sci.*, **41,** 553–574.

——, S. G. Geotis, F. D. Marks and A. K. West, 1981: Winter monsoon convection in the vicinity of north Borneo. Part I: Structure and time variation of the clouds and precipitation. *Mon. Wea. Rev.*, **109,** 1595–1614.

Hsie, E.-Y., R. A. Anthes and D. Keyser, 1984: Numerical simulation of frontogenesis in a moist atmosphere. *J. Atmos. Sci.*, **41,** 2581–2594.

Johnson, R. H., and D. L. Priegnitz, 1981: Winter monsoon convection in the vicinity of north Borneo. Part II: Effect on large-scale fields. *Mon. Wea. Rev.*, **109,** 1615–1628.

——, and D. C. Kriete, 1982: Thermodynamic and circulation characteristics of winter monsoon tropical mesoscale convection. *Mon. Wea. Rev.*, **110,** 1898–1911.

——, and G. S. Young, 1983: Heat and moisture budgets of tropical mesoscale anvil clouds. *J. Atmos. Sci.*, **40,** 2138–2147.

Lacis, A. A., and J. E. Hansen, 1974: A parameterization for the absorption of solar radiation in the earth's atmosphere. *J. Atmos. Sci.*, **31,** 118–133.

Leary, C. A., and R. A. Houze, Jr., 1979: Melting and evaporation of hydrometeors in precipitation from the anvils of deep tropical convection. *J. Atmos. Sci.*, **36,** 669–679.

Lin, Y.-L., R. D. Farley and H. D. Orville, 1983: Bulk parameterization of the snow field in a cloud model. *J. Climate Appl. Meteor.*, **22,** 1065–1092.

Locatelli, J. D., and P. V. Hobbs, 1974: Fallspeeds and masses of solid precipitation particles. *J. Geophys. Res.*, **79,** 2185–2197.

Mason, B. J., 1971: *The Physics of Clouds.* Oxford University Press, 671 pp.

McBride, J. L., and W. M. Gray, 1978: Mass divergence in tropical weather systems. Part II: Large scale controls on convection. *Quart. J. Roy. Meteor. Soc.*, **106,** 517–538.

Miller, M. J., and A. K. Betts, 1977: Traveling convective storms over Venezuela. *Mon. Wea. Rev.*, **105,** 833–838.

Ogura, Y., and M.-T. Liou, 1980: The structure of a midlatitude squall line: A case study. *J. Atmos. Sci.*, **37,** 553–567.

Raymond, D. J., 1975: A model for predicting the movement of continuously propagating convective storms. *J. Atmos. Sci.*, **32,** 1308–1317.

Rodgers, C. D., 1967: The use of emissivity in atmospheric radiation calculations. *Quart. J. Roy. Meteor. Soc.*, **93,** 43–52.

Rutledge, S. A., 1986: A diagnostic modeling study of the stratiform

region associated with a tropical squall line. *J. Atmos. Sci.*, **43**, 1357–1377.

——, and P. V. Hobbs, 1983: The mesoscale and microscale structure and organization of clouds and precipitation in midlatitude cyclones. Part VIII: A model for the "seeder-feeder" process in warm-frontal rainbands. *J. Atmos. Sci.*, **40**, 1185–1206.

——, and R. A. Houze, Jr., 1987: A diagnostic modeling study of the trailing stratiform region of a midlatitude squall line. *J. Atmos. Sci.*, **44**, 2640–2656.

Smull, B. F., and R. A. Houze, Jr., 1987: Dual-Doppler radar analysis of a midlatitude squall line with a trailing region of stratiform rain. *J. Atmos. Sci.*, **44**, 2128–2148.

Sommeria, G., and J. Testud, 1984: COPT 81: A field experiment designed for the study of dynamics and electrical activity of deep convection in continental tropical regions. *Bull. Amer. Meteor. Soc.*, **65**, 4–10.

Soong, S.-T., and W.-K. Tao, 1980: Response of deep tropical clouds to mesoscale processes. *J. Atmos. Sci.*, **37**, 2016–2034.

Stephens, G. L., 1978: Radiation profiles in extended water clouds. Part II: Parameterization schemes. *J. Atmos. Sci.*, **35**, 2123–2132.

——, 1984: The parameterization of radiation for numerical weather prediction and climate models. *Mon. Wea. Rev.*, **112**, 826–867.

——, and P. J. Webster, 1979: Sensitivity of radiative forcing to variable cloud and moisture. *J. Atmos. Sci.*, **36**, 1542–1556.

Webster, P. J., and G. L. Stephens, 1980: Tropical upper-tropospheric extended clouds: Inferences from winter MONEX. *J. Atmos. Sci.*, **37**, 1521–1541.

Zhang, D.-L., and J. M. Fritsch, 1986: Numerical simulations of the meso-β scale structure and evolution of the 1977 Johnstown flood. Part I: Model description and verification. *J. Atmos. Sci.*, **43**, 1913–1943.

——, E.-Y. Hsie and M. W. Moncrieff, 1988: A comparison of explicit and implicit predictions of convective and stratiform precipitating weather systems with a meso-β scale numerical model. *Quart. J. Roy. Meteor. Soc.*, **114**, 31–30.

Zipser, E. J., 1977: Mesoscale and convective-scale downdrafts as distinct components of squall-line circulation. *Mon. Wea. Rev.*, **105**, 1568–1589.